

# Penetration of interferometric radar signals in Antarctic snow

Helmut Rott<sup>1,2,\*</sup>, Stefan Scheiblauer<sup>1</sup>, Jan Wuite<sup>1</sup>, Lukas Krieger<sup>3</sup>, Dana Floricioiu<sup>3</sup>, Paola Rizzoli<sup>4</sup>,  
Ludivine Libert<sup>1</sup>, Thomas Nagler<sup>1</sup>

<sup>1</sup> ENVEO IT GmbH, Innsbruck, Austria

5 <sup>2</sup> Department of Atmospheric and Cryospheric Sciences, Univ. of Innsbruck, Innsbruck, Austria

<sup>3</sup> Remote Sensing Technology Institute, DLR, Oberpfaffenhofen, Germany

<sup>4</sup> Microwaves and Radar Institute, DLR, Oberpfaffenhofen, Germany

\* Correspondence to: Helmut Rott ([helmut.rott@enveo.at](mailto:helmut.rott@enveo.at))

**Abstract.** Synthetic aperture radar interferometry (InSAR) is an efficient technique for mapping the surface  
10 elevation and its temporal change over glaciers and ice sheets. However, due to the penetration of the SAR  
signal into snow and ice the apparent elevation in uncorrected InSAR digital elevation models (DEMs) is  
displaced versus the actual surface. We studied relations between interferometric radar signals and physical snow  
properties and tested procedures for correcting the elevation bias. The work is based on satellite and in-situ data  
15 over Union Glacier in the Ellsworth Mountains, West Antarctica, including interferometric data of the TanDEM-  
X mission, topographic data from optical satellite sensors and field measurements on snow structure and  
stratigraphy undertaken in December 2016. The study area comprises ice-free surfaces, bare ice, dry snow and  
firn with a variety of structural features related to local differences in wind exposure and snow accumulation.  
Time series of laser measurements of NASA's Ice, Cloud and land Elevation Satellite (ICESat) and ICESat-2  
20 show steady state surface topography. For area-wide elevation reference we use the Reference Elevation Model  
of Antarctica (REMA). The different elevation data are vertically co-registered on a blue ice area that is not  
affected by radar signal penetration. Backscatter simulations with a multi-layer radiative transfer model show  
large variations for scattering of individual snow layers but the vertical backscatter distribution can be  
approximated by an exponential function representing uniform absorption and scattering properties. We obtain  
25 estimates of the elevation bias by inverting the interferometric volume correlation coefficient (coherence)  
applying a uniform volume model for describing the vertical loss function. Whereas the mean values of the  
computed elevation bias and the elevation difference between the TanDEM-X DEMs and the REMA show good  
agreement, a trend towards overestimation of penetration is evident for heavily wind-exposed areas with low  
accumulation and towards underestimation for areas with higher accumulation rates. In both cases deviations  
30 from the uniform volume structure are the main reason. In the first case the dense sequence of horizontal  
structures related to internal wind crust, ice layers and density stratification causes increased scattering in near-  
surface layers. In the second case the small grain size of the top snow layers causes a downward shift of the  
scattering phase centre.

## 1. Introduction

Digital elevation models (DEMs) derived from across-track interferometric synthetic aperture radar (InSAR)  
35 data are a main data source for mapping the surface elevation and its temporal change over glaciers and ice  
sheets. Single-pass InSAR (SP-InSAR) systems, such as the TanDEM-X (TDM) mission, are of particular  
interest for this task as they are not affected by variations in the atmospheric phase delay, ice motion and  
temporal decorrelation. For the analysis and interpretation of InSAR elevation over snow and ice the effects of

40 signal penetration have to be taken into account. The surface inferred from uncorrected InSAR elevation data  
refers to the position of the scattering phase centre in the snow/firn medium, resulting in an elevation bias versus  
the actual surface (Dall, 2007). The position and strength of scattering sources in the snow volume and the  
absorption and scattering losses are main factors defining the depth of the phase centre below the snow surface.  
Backscatter contributions from sources in different depths within a volume scattering medium, observed under  
different incidence angles, are causing decorrelation, depending on the interferometric baseline and incidence  
45 angle (Bamler and Hartl, 1988).

Hoehn and Zebker (2000, 2001) derived a formulation for estimating the power-penetration depth in dry snow  
from the interferometric coherence, applying a radiative transfer model for estimating spatial decorrelation in a  
volume of uniformly distributed and uncorrelated scatterers characterized by exponential extinction. They  
applied this formulation to derive the C-band penetration depth for different sites in Greenland from the  
50 coherence of 3-day repeat-pass InSAR data of the ERS-1 SAR mission. Forsberg et al. (2000) and Dall et al.  
(2001) compared surface elevation measured by airborne laser altimetry and C-band single-pass SAR  
interferometry on the Geiki ice cap in Greenland. They report zero InSAR elevation bias for wet snow and an  
average bias of about 10 m for dry snow and firn. Dall (2007) studied relations between the InSAR elevation  
bias and the power penetration depth in uniform volumes. He shows that the depth of the mean phase centre in a  
55 volume scattering medium is approximately equal to the two-way penetration depth if the latter is smaller than  
about 10% of the height of ambiguity ( $H_a$ ), the height difference for a phase shift of  $2\pi$ . Fischer et al. (2019a;  
2019b; 2020) studied various concepts for characterizing and modelling the vertical backscatter distribution and  
retrieving the InSAR penetration bias in the percolation zone of Greenland based on airborne polarimetric multi-  
baseline InSAR data and in situ measurements of snow structural properties.

60 In recent years SP-InSAR data of the TDM mission were widely applied for mapping surface elevation and  
elevation change on glaciers and ice sheets. The TDM mission employs a bi-static interferometric configuration  
of the two satellites TerraSAR-X and TanDEM-X flying in close formation in order to form a single-pass SAR  
interferometer (Krieger et al., 2013). Rizzoli et al. (2017a) compared surface elevation over Greenland measured  
by NASA's Ice, Cloud and land Elevation Satellite (ICESat) laser altimeter with the TanDEM-X global DEM.  
65 They report for frozen snow and firn in the wet snow zone, the lower and upper percolation zone, and the dry  
snow zone mean values of the X-band InSAR penetration bias of 3.7 m, 3.9 m, 4.7 m, and 5.4 m, respectively.  
Abdullahi et al. (2019) use a linear regression model for estimating the elevation bias in TDM DEMs of northern  
Greenland. The model is based on empirical relations between coherence and backscatter intensity with the  
difference between the uncorrected TDM DEMs and airborne laser altimeter surface heights.

70 The complex layered structure of polar snow and firn has a major impact on radar signal propagation and  
interferometric coherence, an obstacle for establishing a generally applicable, physically-based method for  
estimating the elevation bias of InSAR products. The work presented in this paper takes on this open issue,  
exploring relations between interferometric parameters and physical snow properties and investigating the  
feasibility of deducing the elevation bias from the interferometric correlation. The study is based on  
75 interferometric data of the TDM mission, data from optical satellite sensors and field measurements undertaken  
in December 2016 on Union Glacier in the Ellsworth Mountains, Antarctica. Logistic support was provided by  
the private company Antarctic Logistics & Expeditions LLC (ALE) which conducts aircraft flights to Union  
Glacier and operates in summer a field station. The study area comprises ice-free surfaces, bare ice and dry snow

and firm exhibiting a diversity of structural features attributed to local differences in wind exposure and snow accumulation. Time series of ICESat laser measurements from 2003 to 2009 and ICESat-2 data show near steady state surface topography, facilitating the intercomparison of TDM and optical elevation data.

In Sect. 2 we describe the study area, present details on the satellite data base and give an account on the structure and morphology of snow and firm at different sites. Sect. 3 explains the basic concept relating the elevation bias and interferometric coherence in a uniform random volume. Sect. 4 deals with vertical co-registration of the different DEMs, including an analysis of the temporal stability of surface elevation, and describes the observed spatial pattern of the backscatter signals, coherence and elevation bias. Sect. 5 presents results of the inversion of the volumetric coherence in terms of the InSAR elevation bias and compares the retrieved bias with elevation differences between TDM DEMs and optical data. Sect. 6 includes the discussion and Sect. 7 presents conclusions. The Appendix shows simulations for vertical backscatter distributions at snow pit sites and compares these with exponential backscatter functions.

## 2. Study area and data

### 2.1 Surface mass balance and orographic effects

Union Glacier flows from the ice divide in the Heritage Range, Ellsworth Mountains, down to the Constellation Inlet on Ronne Ice Shelf. The glacier section immediately downstream of the main mountain range is exposed to strong katabatic winds so that bare ice appears on the surface (Fig. 1). The blue ice area (BIA) has a negative specific surface mass balance,  $b_n$ , in the order of several centimetres water equivalent (w.e.) per year due to sublimation (Rivera et al., 2014). On the BIA an ice runway for landing heavy airplanes on wheels is maintained from November to March. The ALE camp is located 8 km downstream of the ice runway.

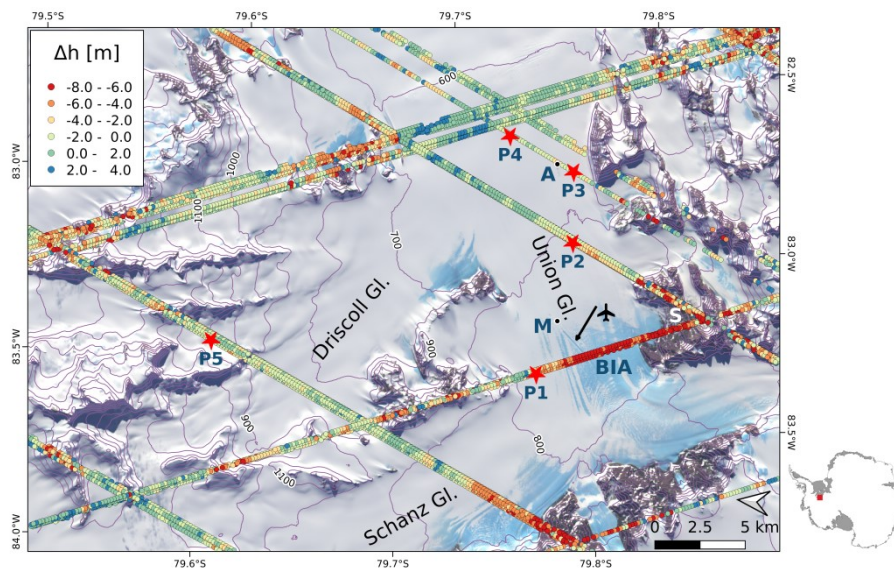


**Figure 1.** Landsat-8 image acquired on 6 December 2016 (composite of bands 5, 4, 2) with ICESat tracks. Points: elevation difference  $\Delta h$  (ICESat minus TDM global DEM), colour coded from  $\Delta h = -8$  m to  $+4$  m. P1 to P5: Locations of snow pits. A – ALE camp, BIA – blue ice area, M – recording meteorological station, S – ice free slope. The arrow points to the landing strip.

GPS measurements at stakes, performed during the period 2007 to 2011, show ice velocities in the order of  $20 \text{ m a}^{-1}$  at the glacier gate across the runway (Rivera et al., 2010; 2014). For 2008 to 2012 a mean wind speed of 16.3 knots with predominant direction from south-west (blowing downstream along the main glacier) was measured

at an automatic station close to the runway. Wind speed and direction are very consistent. Rivera et al. (2014) report a mean  $b_n$  of  $-0.10 \text{ m w.e. a}^{-1}$  measured at 29 stakes on the BIA during 2007 to 2011. The intensity of the katabatic winds declines downstream of the BIA so that snow accumulates and the surface mass balance is positive. Accumulation measurements in 2008-2009 at 4 stakes located on the main glacier 4.5, 7.0, 10.5 and 15 km downstream of the BIA show  $b_n$  values 0.20, 0.13, 0.17 and 0.14  $\text{m w.e. a}^{-1}$  (Rivera et al., 2014). Hoffmann et al. (2020) collected and analysed six shallow ice cores in the wider Union Glacier region. One of the cores was drilled on Union Glacier itself about 2 km west of P3, showing for 1989 to 2013 mean  $b_n$  of  $0.18 \text{ m w.e. a}^{-1}$ .

Differences in the exposure to wind are a main factor for local variations in the accumulation rate and in the structural properties of snow and firn. This is evident in differences of the microstructure and stratigraphy observed in snow pits, ranging from coarse-grained dense snow with wind-crusts near the runway (pit P1), located in the main pathway of the katabatic wind, to finer-grained and softer snow at P5 on a lateral slope of Driscoll Glacier. Accumulation estimates at P5 for 2015 and 2016, deduced from snow pit data, show a mean  $b_n$  of about  $0.4 \text{ m w.e. a}^{-1}$  (Sect. 2.4).

Uribe et al. (2014) operated two radar sensors during an oversnow campaign in December 2010, measuring the total ice thickness and the thickness and structure of the firn layers along an 82 km track, starting on Union Glacier and proceeding along Driscoll and Schanz glaciers up to the Ellsworth Plateau. The total thickness of the firn layer varies significantly along this track, even within short distances. For example, a radargram along a 6 km transect extending from the confluence with Driscoll Glacier across Union Glacier towards the camp shows thickness values of the snow/firn layer ranging from zero on blue ice at the confluence of the two glaciers, increasing gradually with distance to reach a maximum of 34 m close to the camp.

## 2.2 TanDEM-X data

The TDM data for this study comprise one tile of the TDM global (TDMgl) DEM, the primary product of the TDM mission, and raw SAR data from several dates for compiling topography, backscatter intensity and coherence products. We use the TDMgl DEM for topographic corrections and geocoding because it provides full spatial coverage whereas the DEMs of individual dates have gaps, depending on the observation geometry. The data from individual dates are used for studying the impact of specific interferometric configurations on the coherence, backscatter signatures and penetration bias. Tile TDM1\_DEM\_04\_S80W084\_V01\_C of the global DEM is used, extending from  $79^\circ$  to  $80^\circ$  S and  $82^\circ$  to  $84^\circ$  W and referring to the coordinate reference system WGS84-G1150. This tile was obtained by mosaicking multiple single DEM scenes acquired between 6 May 2013 and 23 August 2014. The pixel spacing is 0.4 arcsec in northing and 1.2 arcsec in easting, corresponding to  $12.4 \text{ m} \times 6.5 \text{ m}$  at  $80^\circ$  latitude. For the TDMgl elevation products over ice sheets penetration corrections were applied, using ICESat data as elevation reference (Wessel et al., 2016; Rizzoli et al., 2017b). For Antarctica (excluding coastal regions) a mean penetration bias was derived for each of eleven extended homogeneous areas (fixed blocks) located in different sections of the ice sheet. For the areas in between the elevation is adjusted by spatial interpolation between these blocks, regionally applying bulk values that are not accounting for different surface types (Rizzoli et al., 2017b).

For producing DEMs from raw bistatic SAR data (Level 0) of individual tracks (the so-called Raw DEMs) we used the operational Integrated TanDEM-X Processor (ITP) of the German Aerospace Center (DLR) (Rossi et al., 2012). The Raw DEM pixel spacing is  $6 \text{ m} \times 3 \text{ m}$ . Complementary to each Raw DEM the ITP provides

geocoded rasters of the height error (the Height Error Map, HEM), the SAR amplitude, the backscattering coefficient and the interferometric coherence, as well as a flag mask indicating critical areas. We applied 11 x 11 pixels estimation windows for computing the coherence maps, adding up to about 390 independent samples for single-polarized data at 40° incidence angle and about 110 independent samples for dual-polarized data at 22° incidence angle. According to the Cramér-Rao bound for coherence estimation the standard deviation for a coherence magnitude of 0.5 is 0.03 for the first case and 0.05 for the second case. The uncertainty decreases towards higher coherence values (Bamler and Hartl, 1998). The backscatter intensity images show maps of the normalized radar cross section  $\sigma^\circ$ . For the computation of  $\sigma^\circ$  effects of topography are taken into account for antenna pattern removal and for defining the actual size of the local scattering area. The absolute and relative radiometric accuracies for the TerraSAR-X stripmap data are estimated at 0.6 dB and 0.3 dB, respectively (Breit et al., 2010).

The HEM delivers the height errors for each DEM pixel caused by random noise. It is given by the standard deviation of the interferometric phase for which the coherence and the number of looks are the main factors. The HEM does neither account for the absolute height error (offset) in respect to a particular geodetic reference system nor for penetration related errors. Low pass filtering is an efficient means for reducing the random height error. The HEM for the TDMgl DEM of the study region shows over flat terrain and gentle slopes random height errors ranging from 0.3 m to 1.2 m.

Specifications of the TDM data used in this study are listed in Table 1. The azimuth resolution of the single polarization data is 3.3 m and of the dual polarized data 6.6 m. The ground range resolution is 3.20 m at  $\theta_i = 22^\circ$  and 1.86 m at  $\theta_i = 40^\circ$ . We selected scenes with different incidence angles and baselines in order to check the impact of these parameters on coherence, backscatter intensity and signal penetration. According to the HEM maps, the random errors for the Raw DEMs, excluding steep slopes, range from 0.7 m to 3.0 m. The spatial variations can mainly be attributed to phase noise arising from thermal and volume decorrelation. For the estimation of signal penetration we use averages over multiple pixel windows in order to reduce the uncertainty.

**Table 1.** Specifications of TanDEM-X data used for DEM production and generation of backscatter and coherence images.  $\theta_i$  is the incidence angle in the scene centre.  $B_n$  is the effective interferometric baseline,  $H_a$  is the height of ambiguity,  $k_{zVol}$  is the vertical interferometric wavenumber in the snow volume assuming a density of 400 kg m<sup>-3</sup>. SAR operation mode: bistatic.

Label	Date	Rel. Orbit / Scene	Look direction	Polarisation	$\theta_i$ [deg]	$B_n$ [m]	$H_a$ [m]	$k_{zVol}$ [rad m <sup>-1</sup> ]
T2013A	2013-05-06	105 / 15	Left	HH	40.9	107.4	-65.6	0.111
T2013B	2013-05-22	198 / 14	Left	HH	38.6	106.5	-61.2	0.121
T2014A	2014-05-09	14 / 7	Left	HH	37.5	145.8	-42.9	0.173
T2014B	2014-06-12	233 / 35	Left	HH	40.8	123.5	-56.6	0.128
T2016	2016-12-10	18 / 2	Right	HH & VV	21.6	50.0	-67.3	0.120
T2018	2018-01-10	18 / 2	Right	HH & VV	22.1	30.2	-112.0	0.072

### 2.3 Topographic data from optical satellite sensors

Topographic data from the ICESat and ICESat-2 missions and the Reference Elevation Model of Antarctica (REMA), derived from very high resolution optical stereo images (Howat et al., 2019), are available as reference for estimating the elevation bias in the InSAR DEMs. We use the ICESat and ICESat-2 data primarily for

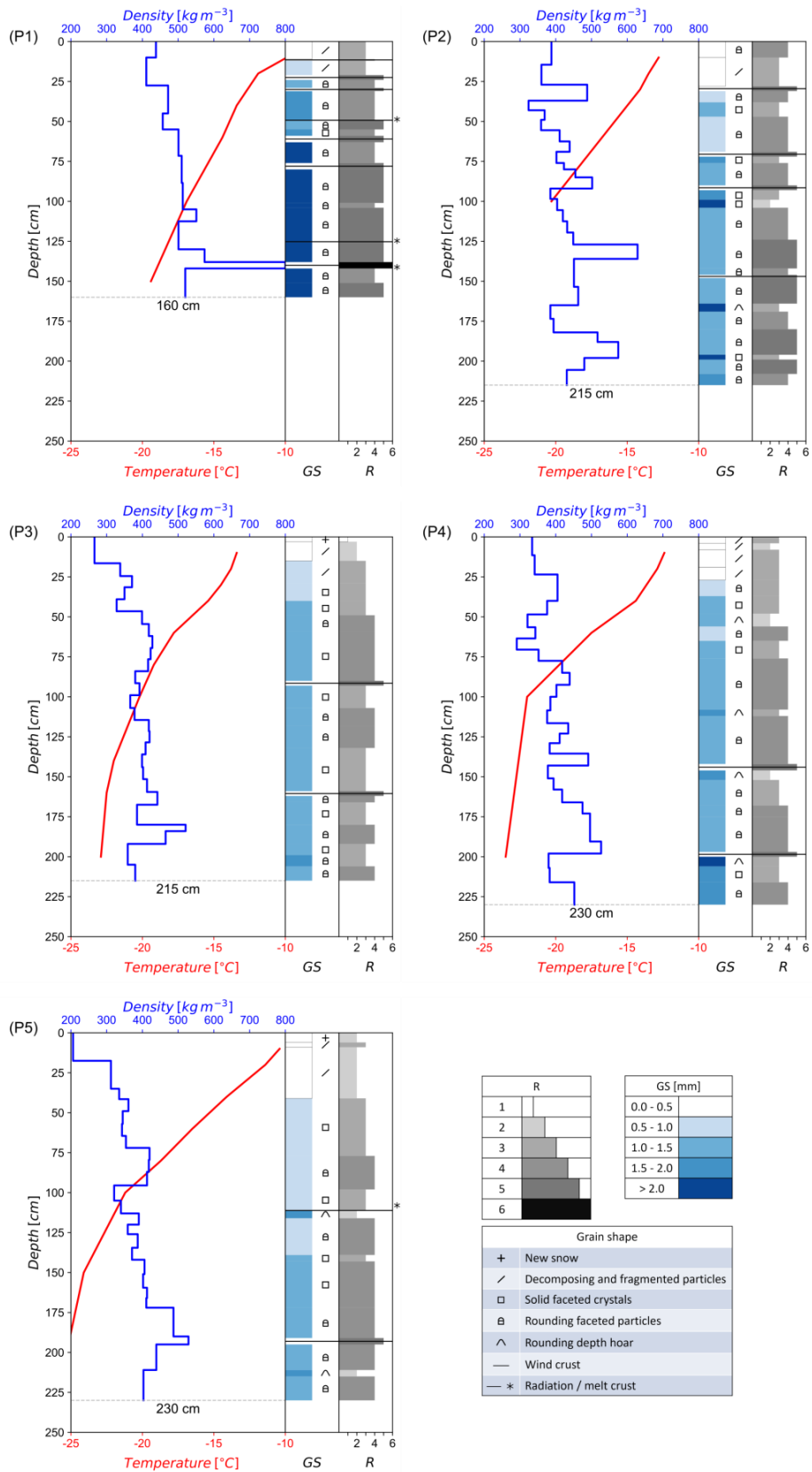
180 assessing the temporal stability of surface elevation. The study area is covered by several tracks of the ICESat  
and ICESat-2 altimeters. Elevation data were acquired by ICESat during several campaigns between April 2003  
and October 2009. We use GLAH12 GLAS/ICESat L2 Global Antarctic and Greenland Ice Sheet Altimetry Data  
(HDF5), Release 34 (Zwally et al., 2014). This product provides geolocated and time tagged surface elevation  
estimates, referenced to the TOPEX/Poseidon ellipsoid, corrected for atmospheric delays and tides. The laser  
footprint size is 60 m to 70 m, the distance between the footprint centres is approximately 170 m. The analysis of  
repeat-track data allows the detection of the surface elevation change after correcting for elevation differences  
185 caused by horizontal shifts of individual footprints. A main cause for the height error of ICESat footprints is the  
uncertainty in beam pointing, causing slope-induced errors (Brenner et al., 2007; Zwally et al., 2011).

Regarding ICESat-2 we use ATLAS/ICESat-2 L3A Land Ice Height, Version 2, Land Ice Along-Track Height  
Product (ATL06), from the time span 2018-10-14 to 2019-09-01. This data set provides geolocated land-ice  
surface heights above the WGS 84 ellipsoid, ITRF2014 reference frame, and ancillary parameters including error  
190 estimates and quality flags (Smith et al., 2019a). ATL06 heights represent the mean surface height averaged  
along 40 m segments of ground track, 20 m apart, for each of the six beams of the Advanced Topographic Laser  
Altimeter System (ATLAS) instrument. The land-ice height is defined as estimated surface height of the segment  
centre for each reference point (Smith et al., 2019b).

For spatially detailed comparisons of elevation we use the REMA DEM Tile Nr. 32-19 with 8 m posting,  
195 covering Union Glacier (Howat et al., 2019). The dates of the image acquisitions for this tile range from January  
2014 to December 2015. The absolute height is based on vertical registration to CryoSat-2 altimetry data,  
acquired in SARIn mode. In order to account for the CryoSat signal penetration a uniform value of 0.39 m was  
added to the CryoSat-2-registered heights over this tile, regardless of the surface type (Howat et al., 2019). This  
needs to be taken into account for using the REMA data as elevation reference because the study area includes  
200 bare ground, ice surfaces, and snow and firn with different structural properties affecting radar signal  
penetration. The vertical error estimates for REMA in the region of interest range from 1.0 m to 1.4 m. The error  
value of each pixel is the standard error from the residuals of the registration to altimetry (Howat et al., 2019).  
The error due to the use of the bulk Cryosat-2 based penetration correction is not included in this error estimate.

## 2.4 Snow pit measurements

205 For the snow pit measurements, made in December 2016, we selected sites covered by ICESat footprints that  
show different values of coherence and backscatter intensity in TDM data. Backscatter properties of dry snow  
and firn are controlled by snow microstructure which is also a main factor for X-band radar signal penetration. In  
the study region the impact of melt for snow metamorphism is marginal. We detected evidence for melt events in  
two of the five snow pits: a thin ice crust in 1.1 m depth in pit 5 and two thin ice crusts along with one ice layer  
210 of 4 cm thickness in pit 1. The temperature record from March 2010 to February 2014 at the meteorological  
station near the runway shows a mean annual air temperature of -21.1 °C and mean monthly temperatures of -8.6  
°C for December and -9.3 °C for January. During those years a few short events with air temperatures close to  
the melting point were recorded.



215 **Figure 2.** Vertical profiles of snow temperature, density, grain size (GS), grain shape and hand hardness (R) for snow pits P1 to P5 on Union Glacier, December 2016. The grain size refers to the maximum axis length of the prevailing snow grains.

Profiles of snow density, temperature, hardness, grain size and shape are shown in Fig. 2. The pits vary in depth between 1.6 m and 2.3 m. The observed grain size refers to the maximum axis length of prevailing grains (Fierz et al., 2009). Hardness was estimated by the hand test, ranging from very low (R1) to very high (R5) for snow and R6 for ice. The mean density of snow/firn for layers of 0.5 m vertical extent is specified in Table 2. Grain size and hardness show significant differences between the five measurement sites. The size and shape of the snow grains and the sequence and properties of snow/firn layers are arising from accumulation history, exchange processes of radiation, turbulent heat and mass at the snow/air interface, and vapour diffusion in the snow volume. Down to about 2 m depth the temperature gradient metamorphism is the dominating process for grain growth, triggered by seasonal temperature variations (Alley, 1988; Colbeck, 1983). Average temperature gradients in the top metre of the five snow pits were in the order of 10 °C m<sup>-1</sup>. Differences in the average grain size of the pits can, at least partly, be attributed to the snow age following from differences in the surface mass balance (Sect. 2.1). Courville et al. (2007) studied the microstructure of snow and firn in a megadune region in East Antarctica. They show that local differences in grain size, thermal conductivity, and permeability are related to spatial accumulation variability in which already relatively small differences in the net accumulation due to wind redistribution cause significant differences of physical snow properties.

**Table 2.** Mean density of snow/firn for layers of 0.5 m vertical extent of snow pits P1 to P5 on Union Glacier. The snow pit altitude refers to the REMA DEM.

	P1	P2	P3	P4	P5
Altitude [m]	756.8	690.1	674.1	656.0	1133.3
Depth	Snow density [kg m <sup>-3</sup> ]				
0 to 0.5 m	443	390	323	366	286
0.5 to 1.0 m	499	422	408	369	372
1.0 to 1.5 m	548	471	399	408	371
1.5 to 2.0 m		467	419	472	451

Snow pit 1 exhibits the largest grains, the highest snow density, thin ice layers and several wind crusts. Accumulation data are not available, but from the closeness to the BIA it can be concluded that the mean accumulation rate is well below the accumulation rate near the ALE camp. Due to the high exposure to katabatic winds the stratification does not allow an identification of annual accumulation layers. In some years sublimation and wind erosion may result in negative mass balance. The higher hardness values compared to the other sites can be attributed to more frequent exposure to high wind speeds, the erosion and deposition of blowing snow and greater age due to low accumulation. Two thin ice crusts (5 mm thickness) at 0.49 m and 1.25 m depth are possibly tracing back to radiation penetration causing melt below the frozen surface (Colbeck, 1989). An ice layer of 4 cm thickness between 1.38 and 1.42 m depth, with air bubbles of up to 2 mm size, indicates an intensive melt event.

P2 is the snow pit with the highest average snow density next to P1. It is located half-way between the runway and the ALE camp, more exposed to katabatic winds than the camp so that the average accumulation rate should be lower than at P3 and P4. The stratigraphy down to 2 m depth shows four layers of high density with comparatively fine-grained snow, typical for wind packs, and several thin wind crusts. Softer layers with faceted grains show up below wind packs, but a clear assignment to seasonal or annual layers is not possible.



250 The pits P3 and P4, located in the vicinity of the camp, show lower mean density and less variations of density with depth. P4 is located slightly upstream of stake B10 for which Rivera et al. (2014) report a specific mass balance  $b_n = 0.17 \text{ m w.e. a}^{-1}$  for 2008-2009. Down to the depth of 2.0 m the P4 stratification shows four comparatively thick, hard layers with rounding depth hoar below. The total snow mass down to 2.0 m amounts to 0.81 m w.e. Assuming that the transitions from hard to soft layers corresponds to late summer horizons and  
 255 accounting for the lack of two months to cover the full 4-year period implies an annual accumulation rate  $b_n = 0.21 \text{ m w.e. a}^{-1}$ . At P3 the sequence of layers is less distinct. This site is located in 300 m cross-wind distance of the camp and may be affected by local perturbations of snow drift during summer when the camp is set up in full extent.

P5 is located at 1133 m elevation on a flat section of a slanting lateral branch of Driscoll Glacier that extends  
 260 uphill towards the Pioneer Heights, 400 m in altitude above the confluence with Union Glacier. The site is not exposed to the strong katabatic winds that are blowing along the main branch of Union Glacier. The grain size is smaller and the snow is softer than at the other sites. A melt crust of 3 mm thickness was found in 1.14 m depth, most likely related to a short event with comparatively warm temperatures on 17-18 January 2016. The snow mass above this crust amounts to 0.38 m w.e. A thin hard layer in 2.11 m depth with a soft, coarse-grained layer  
 265 below refers probably to the 2015 late-summer horizon. The snow mass between the wind crust in late summer 2015 and the melt crust in January 2016, a period of about 11 months, amounts to 0.41 m w.e. These two accumulation estimates indicate for this site about twice the accumulation rate on the main glacier near the ALE camp.

### 3. Interferometric coherence and penetration-related elevation bias

270 The procedure for estimating the interferometric elevation bias is based on the inversion of the volumetric correlation factor which can be derived from total coherence products ( $\gamma_{tot}$ ) generated during InSAR processing. The total interferometric complex correlation coefficient (coherence) of a random medium is made up by the following contributions (Krieger et al., 2007):

$$\gamma_{tot} = \gamma_{therm} \cdot \gamma_{Quant} \cdot \gamma_{Amb} \cdot \gamma_{Rg} \cdot \gamma_{Az} \cdot \gamma_{Vol} \cdot \gamma_{temp} \quad (1)$$

275 The terms on the right-hand side refer to the interferometric correlation coefficient related to the signal-to-noise ratio ( $\gamma_{therm}$ ), quantization ( $\gamma_{Quant}$ ), azimuth and range ambiguities ( $\gamma_{Amb}$ ), baseline decorrelation ( $\gamma_{Rg}$ ), relative shift of the Doppler spectra ( $\gamma_{Az}$ ), volumetric decorrelation ( $\gamma_{Vol}$ ), and temporal decorrelation ( $\gamma_{temp}$ ). Temporal decorrelation is not relevant for SP-InSAR data over ground, including snow and ice ( $\gamma_{temp} = 1.0$ ).

The thermal interferometric correlation component is related to the signal-to-noise ratio (SNR) of the two SAR  
 280 images by:

$$\gamma_{therm} = \frac{1}{\sqrt{(1 + SNR_1^{-1})(1 + SNR_2^{-1})}} \quad (2)$$

For SP-InSAR the volumetric correlation coefficient can be derived from the total coherence by:

$$\gamma_{Vol} = \frac{\gamma_{tot}}{\gamma_{therm} \gamma_{Quant} \gamma_{Amb} \gamma_{Rg} \gamma_{Az}} \quad (3)$$

The phase noise due to  $\gamma_{Amb}$ ,  $\gamma_{Quant}$  and  $\gamma_{Az}$  of advanced SAR systems is small. For TDM SP-InSAR  
 285 interferograms Krieger et al. (2007) estimate the typical loss in coherence for each of the terms  $\gamma_{Amb}$ ,  $\gamma_{Quant}$  and  
 $\gamma_{Az}$  at  $< 2\%$ . Baseline decorrelation,  $\gamma_{Rg}$ , is avoided by applying common bandwidth filtering.

Hoen and Zebker (2000) specify a formulation for the correlation factor in a uniform volume with exponential  
 extinction in which the interferometric phase is proportional to the penetration length,  $d_i$ :

$$\gamma_{Vol} = \frac{1}{\sqrt{1 + \left(\frac{p\pi\sqrt{\epsilon}d_iB_n}{r_0\lambda\tan\theta_i}\right)^2}} = \frac{1}{\sqrt{1 + \left(\frac{\pi\sqrt{\epsilon}d_i\cos\theta_i}{H_a}\right)^2}} \quad (4)$$

290  $\lambda$  is the radar wavelength,  $r_0$  is the slant range distance,  $\theta_i$  is the incidence angle at the air/snow interface,  $B_n$  is  
 the effective interferometric baseline,  $\epsilon$  is the dielectric permittivity.  $p = 1$  is valid for the combination of one  
 monostatic and one bi-static SAR image forming an interferogram,  $p = 2$  for the combination of two monostatic  
 images.  $H_a$  is the height of ambiguity in free space:

$$H_a = \frac{\lambda r_0 \sin\theta_i}{p B_n} \quad (5)$$

295 According to the radiative transfer approach the one-way power penetration length  $d_l$  [m], where the intensity of  
 the signal is attenuated to  $1/e$  of the incident signal, is given by

$$d_l = \frac{1}{k_e} = \frac{1}{k_s + k_a} \quad (6)$$

where  $k_a$  and  $k_s$  [ $m^{-1}$ ] are the absorption and the scattering coefficients. The one-way power penetration depth,  $d_p$ ,  
 referring to vertical direction is obtained by accounting for the refraction angle  $\theta_r$ :

$$300 \quad d_p = d_l \cos\theta_r. \quad (7)$$

The vertical interferometric wavenumber,  $k_z$  [ $rad\ m^{-1}$ ], relates the phase of the interferometric correlation to the  
 geometric configuration of the interferometer, providing phase ( $\varphi$ ) to height conversion:

$$k_z = \frac{\partial\varphi}{\partial z} = \frac{2\pi}{H_a} \quad (8)$$

The wavenumber in a lossy volume accounts for the change in the propagation constant and refraction (Lei et al.,  
 305 2016), yielding the following formulation for the height of ambiguity in the volume:

$$H_{aVol} = \frac{2\pi}{k_{zVol}}, \text{ where } k_{zVol} = k_z \sqrt{\epsilon} \frac{\cos\theta_i}{\cos\theta_r} = \quad (9)$$

For dry snow and ice the absorption losses are very small so that the real part of the permittivity can be used  
 (Mätzler, 1996). In Table 1 the values for  $H_a$  and for  $k_{zVol}$  (assuming a snow density of  $400\ kg\ m^{-3}$ ) are specified  
 for the TDM scenes.

310 Dall (2007) shows that the penetration-related elevation bias,  $h_b$ , is approximately equal to the two-way power  
 penetration depth,  $d_{p2}$ , if the latter is small compared to  $H_{aVol}$ . For large relative penetration depths ( $d_{p2}/H_{aVol}$ ) the  
 elevation bias approaches one quarter of the ambiguity height. Normalizing the coherence phase,  $\angle\gamma$ , by the  
 interferometric phase at the volume surface ( $\angle\gamma = \varphi - \varphi_{surface}$ ) yields the following relation in which the elevation  
 bias is proportional to  $\angle\gamma$  (Dall, 2007):

315 
$$h_b = \angle\gamma / k_{zVol} = \angle\gamma |H_{aVol}| / 2\pi \quad (10)$$

For a uniform volume a direct relationship between the coherence magnitude and the relative penetration depth can be defined from which the phase can be computed (Dall, 2007):

$$\angle\gamma = -sgn(H_{aVol}) \arctan(\sqrt{|\gamma_{Vol}|^{-2} - 1}) \quad (11)$$

320 As according to this relation the coherence phase is uniquely defined by the coherence magnitude, the following formulation can be used for estimating the elevation bias:

$$h_b = -\left|\frac{H_{aVol}}{2\pi}\right| \arctan(\sqrt{|\gamma_{Vol}|^{-2} - 1}) \quad (12)$$

We apply this equation for estimating the elevation bias from the observed coherence, using the magnitude of the volumetric InSAR correlation factor as input. According to this formulation the actual InSAR elevation bias becomes progressively smaller than  $d_{p2}$  with increasing relative penetration depth.

325 This approach is based on the assumption of a uniform volume with exponential extinction whereas dry polar firn is a density stratified medium featuring distinct differences of scattering and extinction properties between individual layers, as well as depth-dependent changes. However, for inverting the observed interferometric coherence in terms of the elevation bias the assumption of a simple model is needed for describing the vertical backscatter and extinction properties. We tested the applicability of the uniform volume approach for describing  
330 the observed backscatter intensity, performing forward computations with a multi-layer radiative transfer model (see Appendix).

#### 4. Analysis of backscatter signatures, coherence and elevation bias

In this section we show the spatial pattern of backscatter intensity and coherence in the study area and relations of these parameters to the elevation bias inferred from optical sensor data. We start with an account on  
335 topographic reference data and the procedures applied for vertical co-registration, a critical step for estimating the penetration-related elevation bias.

##### 4.1 Topographic reference and vertical co-registration

The precise vertical co-registration on surfaces that are not subject to radar signal penetration is essential for obtaining reliable estimates on the interferometric elevation bias. If the data to be co-registered are lacking  
340 temporal coincidence, checks on the temporal stability of the surfaces are needed. These topics are addressed below.

##### 4.1.1 Notations for elevation differences

The apparent glacier surface in an InSAR DEM refers to the position of the scattering phase centre in the snow and firn volume. The elevation bias,  $h_b$ , is the difference between the apparent elevation derived by means of the  
345 InSAR method,  $h_{insar}$ , and the true surface elevation,  $h_s$ :

$$h_b = h_{insar} - h_s. \quad (13)$$

For the elevation bias estimate derived from the volumetric coherence by means of Eq. (12) we use the notation  $h_{blnv}$ . For studying the penetration-related elevation bias we co-register the TDM DEMs on surfaces devoid of penetration with elevation data of optical sensors. On these surfaces the raw TDM DEMs show vertical offsets up to a few metres because for these data only a preliminary adjustment for absolute height is performed with ITP processing. We use the notation  $\Delta h$  for specifying the elevation difference between optical data and the un-registered TDM DEMs on surface scattering targets:

$$\Delta h = h_{optical} - h_{TDM,unreg} \quad (14)$$

Suitable targets for vertical co-registration in the study area are the BIA and bare ground on an ice-free slope bordering the BIA (“S” in Fig. 1). We use the notation  $dh$  for the elevation difference between the TDM DEMs and optical elevation data, vertically co-registered on surface scattering targets:

$$dh = h_{TDM,coreg} - h_{optical} \quad (15)$$

In case of temporal coincidence or stable topography  $dh$  corresponds to the interferometric elevation bias. Though the time series of ICESat data indicate temporal stability of surface elevation in the study area, minor errors due to temporal changes in elevation cannot be fully excluded.

#### 4.1.2 Temporal stability of surface elevation

Because of the lack in temporal coincidence between the TDM and optical elevation data we checked the temporal variability using ICESat time series. The main section of the BIA was crossed by ICESat repeat tracks on seven dates between May 2004 and November 2009 (Fig. 1). The mean difference in elevation  $\Delta h$  between the ICESat footprints on the BIA and the corresponding TDMgl cells (mean values of 5 x 5 pixels) is -6.76 m. The standard deviation for the 126 samples of the time series is 0.43 m (Table S1 in the Supplement). The mean  $\Delta h$  values on the different dates range from -6.61 m to -6.86 m without any distinct temporal trend, indicating high temporal stability. The stability of surface elevation on the BIA is also confirmed by the GPS time series of Rivera et al. (2014). The  $\Delta h$  value of -6.76 m can be mainly attributed to the bulk penetration correction that is applied for TDMgl DEM products over Antarctica. The ICESat-2 data set of the BIA includes eight tracks with altogether 345 spots, extending along the eastern and western margins of the BIA which are occasionally covered by snow. The mean elevation difference and standard deviation are:  $\Delta h(\text{ICESat-2-TDMgl}) = -6.99$  m,  $\sigma_{\Delta h} = 0.38$  m.

In order to check the validity of the assumption that the BIA signal arises from surface scattering we derived optical - SAR elevation differences also on the ice-free slope in the vicinity of the BIA. This slope has a mean inclination of about 16 degrees and contains sections of varying steepness. On slopes horizontal shifts between pixels to be co-registered cause slope-dependent elevation biases, in particular for data from sensors with different observation geometries and spatial resolution (Nuth and Kääb, 2011). Therefore we use data from moderately inclined slope sections for quantifying the vertical offsets. In order to avoid steep slope sections we excluded all cells of 5 x 5 TDM pixels with a standard deviation of elevation larger than 5 m. Under this constraint only 21 ICESat pixels of the whole time series qualify for the comparison on the slope, yielding a mean  $\Delta h$  of -6.91 m and  $\sigma_{\Delta h}$  of 0.84 m. The difference of the mean  $\Delta h$  values between the slope and the BIA is below the measurement uncertainty.

Another ICESat time series for checking the temporal behaviour of surface elevation extends across the main glacier near pit 4 where the penetration bias is several metres. The ICESat data set comprises seven closely-spaced tracks acquired between 11 April 2003 and 12 February 2008. The mean value and standard deviation of the elevation difference between ICESat and the TDMgl DEM are on the central section of the glacier:  $\Delta h = 0.09$  m,  $\sigma_h = 0.40$  m (Table S2). The mean  $\Delta h$  values on individual dates range from -0.03 m to 0.21 m without any obvious temporal trend, confirming also the temporal stability of surface elevation. Subtracting the TDMgl offset of -6.76 m from the mean  $\Delta h$  value (0.09 m) yields an elevation bias (dh) of -6.67 m due to signal penetration.

#### 4.1.3 Vertical co-registration of the DEMs

We use REMA elevation data as reference in order to obtain spatially detailed estimates of the interferometric elevation bias. The mean value and standard deviation of the elevation difference between ICESat and REMA over the BIA are:  $\Delta h = -0.33$  m,  $\sigma_{\Delta h} = 0.38$  m (Table S1). This value differs by 6 cm from the bulk penetration correction (-0.39 m) that was applied to CryoSat-2 elevation data used as absolute height reference for the REMA DEM (Howat et al., 2019). This correction introduces a bias over bare ice where the actual CryoSat-2 signal refers to surface reflection. On the ice-free slope the elevation differences of REMA versus ICESat, ICESat-2 and TDMgl elevation data show high standard deviations. Therefore we use the BIA as reference site for vertical co-registration between the TDM DEMs and REMA.

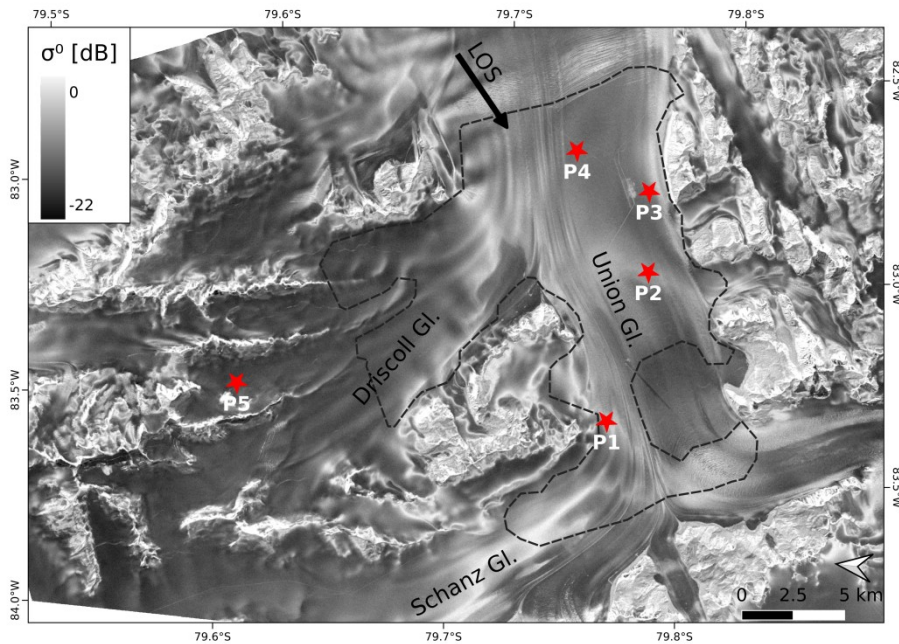
For cross-comparing the TDM and REMA elevation data we outlined an area of 5 km<sup>2</sup> extent in the central section of the BIA that is crossed by the ICESat tracks, avoiding BIA sections that are occasionally covered by snow. The mean elevation difference  $\Delta h$  between REMA and TDMgl is -6.37 m, the standard deviation at 8 m x 8 m pixel size is 0.62 m. We use the value of -6.37 m for vertical co-registration of the TDMgl DEM. The same polygon is used for vertical co-registration of the other TDM DEMs which as un-registered DEMs show vertical shifts vs. REMA of -2 m to -3 m.

#### 4.2 Spatial pattern of backscatter signals and coherence

Fig. 3 shows an image of the backscatter cross section ( $\sigma^\circ$ ) and Fig. 4 an image of the magnitude of the complex interferometric correlation coefficient (the total normalized coherence), derived from TDM data of 6 May 2013 (scene T2013A). The outline encloses the level glacier area (LGA) excluding blue ice areas and slopes larger than 5° inclination, confining the data used for the statistical analysis of signatures and elevation bias in firm areas (Table 3). Major blue ice areas are located in the vicinity of the landing strip, on Schanz Glacier and at the confluence of Driscoll and Union glaciers. The LGA area is completely covered by each of the TDM scenes listed in Table 1. The slope constraint reduces impacts of errors in optical and SAR DEM co-registration and effects of fore-slopes and layover related to different SAR observation geometries.

The spatial pattern of backscatter intensity on the firm areas of the main glacier and its tributaries reflects primarily differences in volume scattering properties and to some extent also the pattern of the elevation bias (Sect. 5). Low  $\sigma^\circ$  values on the LGA refer to areas of comparatively fine grained snow and firm in the top layers, whereas high values are an indication for large scattering elements. The blue ice areas have a comparatively smooth surface, accounting for low  $\sigma^\circ$  at an incidence angle of 40°. The lowest  $\sigma^\circ$  values show up on tributary glaciers away from the main passage of the katabatic wind. Low  $\sigma^\circ$  is also evident at locations of increased accumulation rates in the vicinity of the camp. At lower incidence angles  $\sigma^\circ$  is higher throughout and the overall

dynamic range of  $\sigma^\circ$  is reduced, as evident in Fig. S1 which shows backscatter and coherence images of 10 December 2016.



425 **Figure 3.** Section of TDM backscatter image, HH polarization, 6 May 2013. LOS (line of sight) indicates the radar look direction. The outline encloses the LGA. Incidence angle in the scene centre ( $\theta_i$ )  $40.9^\circ$ .

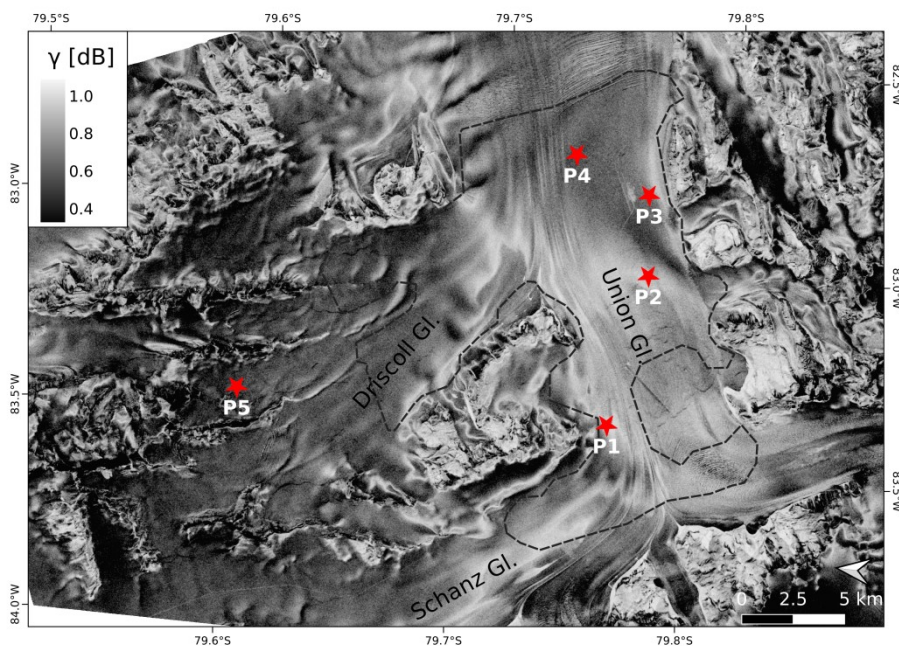


**Figure 4.** Image of total normalized coherence,  $\gamma_{tot}$ , from the TDM interferogram of 6 May 2013.

The incidence angle dependence of  $\sigma^\circ$  in the vicinity of the BIA and in crevasse zones is rather small (Fig. 5). In these areas the differences in  $\sigma^\circ$  between the scenes T2013A ( $\theta_i = 40.9^\circ$ ) and T2016H ( $\theta_i = 21.6^\circ$ ) amount to about 3 dB and  $\sigma^\circ$  is high in both scenes. This is an indication for large scattering elements relative to the wavelength. Multiple scattering between individual layers and scattering at rough internal interfaces may also play a role. In the areas with higher accumulation rates the incidence angle dependence is larger, reaching values

up to 8 dB in the vicinity of pit 4. Large angular backscatter differences of the stratified snow/firn medium can be explained by increased backscatter contributions of internal interfaces towards near-nadir angles. The pronounced  $\sigma^\circ$  increase towards low incidence angles on the BIA (-13.3 dB in scene T2013A, -5.9 dB in T2016H) is characteristic for backscattering of slightly rough surfaces (Fung, 1994).

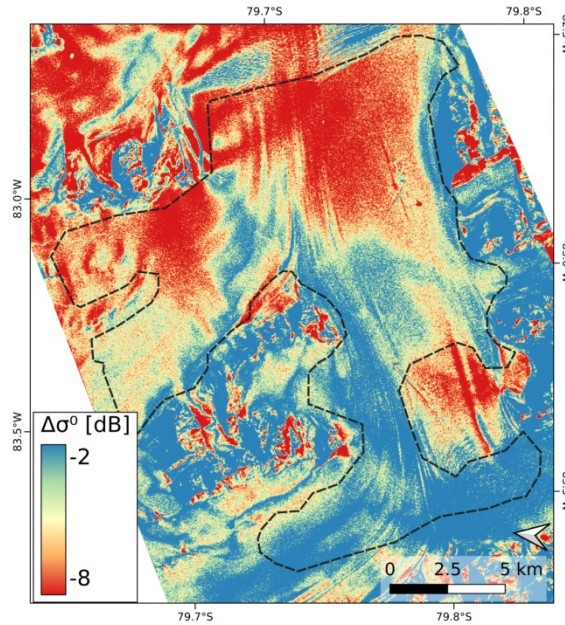


**Figure 5.** Difference of the HH-polarized backscatter coefficients between the TDM images from 6 May 2013 ( $\theta_i = 40.9^\circ$ ) and 10 December 2016 ( $\theta_i = 21.6^\circ$ ),  $\sigma_{HH}^\circ$  2013 minus  $\sigma_{HH}^\circ$  2016 [dB].

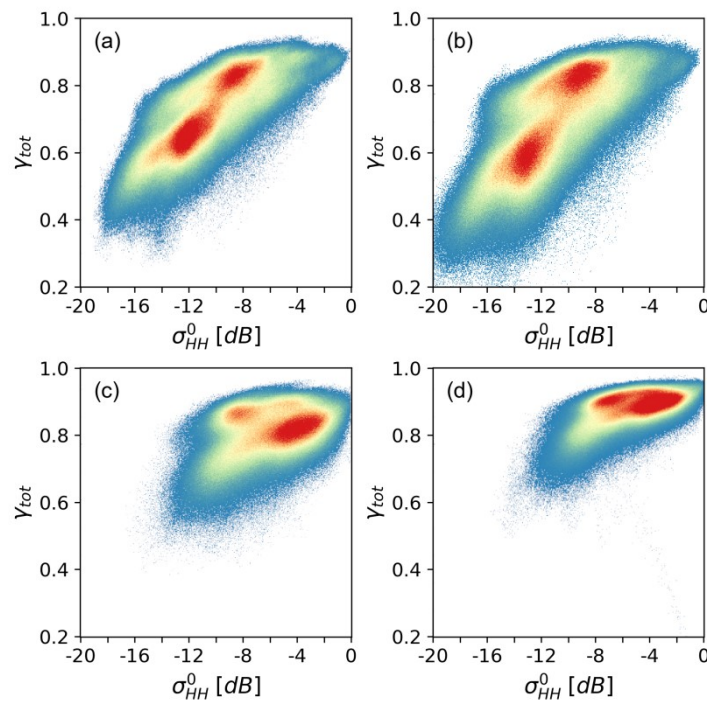


**Figure 6.** Scatterplot of the backscatter coefficient  $\sigma_{HH}^\circ$  [dB] vs. the total normalized coherence,  $\gamma_{tot}$ , for the level glacier area (LGA). (a) 6 May 2013 ( $\theta_i = 40.9^\circ$ ); (b) 22 May 2013 ( $\theta_i = 38.6^\circ$ ); (c) 10 December 2016 ( $\theta_i = 21.6^\circ$ ); (d) 10 January 2018 ( $\theta_i = 21.1^\circ$ ). The colour represents the 2D data density increasing from blue to red. The reduced range of coherence in (d) compared to (c) can be attributed to the shorter effective baseline.

The coherence image of 6 May 2013 (Fig. 4) shows the lowest coherence on glacier sections with the largest elevation bias located on Driscoll Glacier and near the ALE camp ( $\gamma_{\text{tot}} = 0.50$  to  $0.65$ ). In the T2013 and T2014 (T2013/14) TDM images the coherence of the BIA is also comparatively low (mean  $\gamma_{\text{tot}} = 0.79$ ) because of thermal decorrelation due to the low SNR. In the low accumulation areas surrounding the BIA the  $\sigma^\circ$  values range from  $-5$  dB to  $-8$  dB and the magnitude of  $\gamma_{\text{tot}}$  ranges from  $0.85$  to  $0.90$ . The incidence angle has also an impact on the relation between coherence and  $\sigma^\circ$ . This is evident by comparing scatterplots of scenes with different incidence angles (Fig. 6). The two scenes with  $40.9^\circ$ , respectively  $38.6^\circ$  incidence angle show an approximately linear relation between coherence and  $\sigma^\circ$  with two cluster centres corresponding to the surroundings of the BIA respectively to areas with higher accumulation rates. The scenes with  $22^\circ$  incidence angle (T2016/18) show reduced dynamic range of coherence and  $\sigma^\circ$ . The volumetric normalized coherence, derived from the observed total coherence according to Eq. (3), shows the expected trend, i.e. decrease of  $\gamma_{\text{Vol}}$  with increasing baseline (decreasing  $H_a$ ) height of ambiguity at a given incidence angle (Table 3). The lowest mean coherence value over the LGA is observed for scene T2014A ( $|H_a| = 42.9$  m,  $\gamma_{\text{Vol}} = 0.656$ ).

**Table 3.** Mean values over the level glacier area (LGA) for the elevation difference TDM - REMA (dh), the TDM elevation bias by inversion of volumetric coherence ( $h_{\text{bInv}}$ ), the difference between dh and  $h_{\text{bInv}}$ , the volumetric coherence ( $\gamma_{\text{Vol}}$ ) and the backscatter coefficient ( $\sigma^\circ$ ).  $R^2$  is the coefficient of determination for linear correlation between  $d_h$  and  $h_{\text{bInv}}$ , RMSD is the root mean square difference between  $d_h$  and  $h_{\text{bInv}}$ .

	T2013A	T2013B	T2014A	T2014B	T2016H	T2016V	T2018H	T2018V
dh [m]	-5.97	-5.63	-5.49	-5.10	-4.28	-4.48	-4.78	-4.82
$h_{\text{bInv}}$ [m]	-5.80	-5.43	-4.85	-4.78	-4.39	-4.40	-5.17	-5.19
dh - $h_{\text{bInv}}$ [m]	-0.17	-0.20	-0.64	-0.32	0.11	-0.08	0.39	0.37
$\gamma_{\text{Vol}}$	0.791	0.778	0.656	0.808	0.864	0.858	0.927	0.926
$\sigma^\circ$ [dB]	-9.37	-9.95	-8.21	-9.12	-5.21	-5.36	-4.49	-4.71
$R^2$	0.57	0.59	0.47	0.49	0.41		0.27	
RMSD [m]	1.88	1.84	2.03	1.56	1.43		1.79	

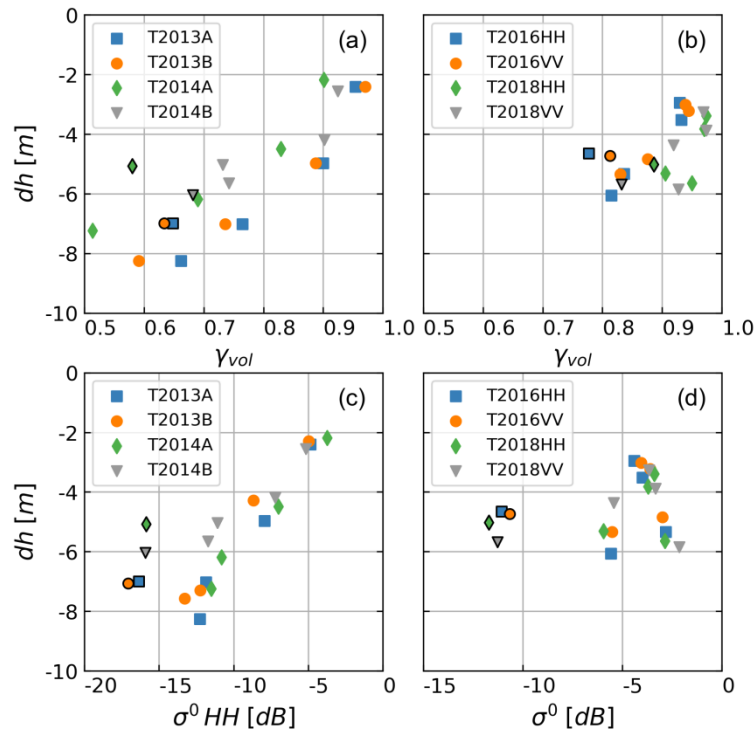
### 4.3 Backscatter signatures, coherence and elevation bias at the snow pit sites

The backscatter coefficients, the magnitude of the total and volumetric correlation coefficients and the elevation bias for cells with 90 m diameter centred at the snow pit sites are listed in Tables S3 and S4. The speckle related uncertainty (standard deviation) of  $\sigma^\circ$  for the 90 m cells is 0.13 dB for the single polarized data at  $\theta_i = 40^\circ$  (T2013/14 scenes) and 0.26 dB for the HH and VV polarized data at  $\theta_i = 22^\circ$  (T2016/18 scenes). The  $\gamma$ -values are based on the coherence pixels whose centre coordinates fit within the corresponding 90 m cell. Pit 5 is not covered by the scenes T2016 (10 December 2016) and T2018 (10 January 2018). We derived the data for Pit 5 from two scenes of adjoining tracks with similar height of ambiguity and incidence angle: 7 January 2017 ( $\theta_i = 24.6^\circ$ ,  $H_a = -70.0$  m) and 16 January 2018 ( $\theta_i = 24.7^\circ$ ,  $H_a = -106.0$  m).

Fig. 7 shows plots of the volumetric coherence and the backscatter coefficient versus the elevation difference dh between the TDM DEMs and the REMA at the snow pit sites. In order to point out effects of the incidence angle the data derived from the T2013/14 and from the T2016/18 scenes are displayed separately. There is a clear trend



475 of decrease in  $\gamma_{vol}$  with increasing magnitude of  $dh$ . The scene T2014A with the largest  $|H_a|$  shows the highest sensitivity of  $\gamma_{vol}$  in respect to  $dh$ , and the scene T2018 with the shortest  $|H_a|$  shows the lowest sensitivity.



480 **Figure 7.** Relations between the elevation difference ( $dh$ ) TDM - REMA and volumetric coherence (a) (b), respectively the backscatter coefficient (c) (d) for the snow pit sites P1 to P5. The framed points refer to P5. Incidence angle in the swath centre: (a) and (c)  $\theta_i = 37.5^\circ$  to  $40.9^\circ$ , (b) and (d)  $\theta_i = 21.6^\circ$  and  $22.1^\circ$ .

The incidence angle has also an effect on the elevation bias. For example, the two scenes with almost the same height of ambiguity show different mean  $dh$  values of the snow pit sites (Table S4), T2013A:  $|H_a| = 65.6$  m,  $\langle dh \rangle = 5.93$  m; T2016:  $|H_a| = 67.3$  m,  $\langle dh \rangle = 4.35$  m. The same behaviour is evident for the mean  $dh$  of the LGA (Table 3):  $\langle dh \rangle = 5.97$  m for T2013A and  $\langle dh \rangle = 4.38$  m for T2016.

485 Regarding polarization, there are no significant differences between HH and VV polarized data for  $\gamma_{vol}$  and  $dh$ . Whereas the snow pit sites show slightly larger  $|dh|$  at HH polarization, over the LGA this is the case at VV polarization. The differences in  $\sigma^\circ$  and coherence between HH and VV polarization are also small. The average  $\sigma^\circ_{HH}$  of the snow pit sites is 0.28 dB lower than  $\sigma^\circ_{VV}$ .

490 The plots of  $dh$  vs.  $\sigma^\circ$  at the snow pits in Fig. 7 indicate for the T2013/14 scenes an approximately linear relation for the sites P1 to P4, but the data of P5 ( $\langle \sigma^\circ \rangle = -16.3$  dB) are shifted by a few dB. The reduced  $\sigma^\circ$  of P5 can be attributed to the smaller grain size and a smoother vertical density profile. The T2016/18 data do not show any obvious relation between  $dh$  and  $\sigma^\circ$ . P4 with ( $\sigma^\circ_{HH} -2.8$  dB) and P5 ( $\sigma^\circ_{HH} -11.0$  dB) have a similar elevation bias. The same behaviour as for P4, with comparatively deep penetration and high  $\sigma^\circ$  in the T2016/18 data, is evident for an extended area in its surroundings which shows high backscatter in the T2016/18 data (mean  $\sigma^\circ = -3$  dB) and a comparatively large elevation bias (mean  $dh = -5$ m). The high  $\sigma^\circ$  at near nadir angles is an indication for increased backscatter at internal interfaces, but it is not clear why this has less impact on volume decorrelation.

## 5. Estimation of the interferometric elevation bias

Building on the signature analysis reported in Sect. 4, we focus on the use of the volumetric coherence for estimating the interferometric elevation bias by inverting  $\gamma_{Vol}$  according to Eq. (12). For computing the vertical wavenumber in the volume and the refraction angle we assume a snow density of  $400 \text{ kg m}^{-3}$ , resulting in  $\epsilon' = 1.763$  (Mätzler, 1996). Fig. 8 shows plots of the computed elevation bias,  $h_{bInv}$ , at the snow pit sites derived from  $\gamma_{Vol}$  vs. the elevation difference  $dh$  between the InSAR DEMs and the REMA. The T2013/14 data show a highly significant linear relation between  $dh$  and  $h_{bInv}$ , with a coefficient of determination  $R^2 = 0.86$ . The root-mean-square difference (RMSD) is 0.74 m, attributed to errors of the computed  $h_{bInv}$  and the DEM difference product. The T2016/18 data (mean of HH and VV polarization) show a linear relation with  $R^2 = 0.59$ , the RMSD is 0.84 m.

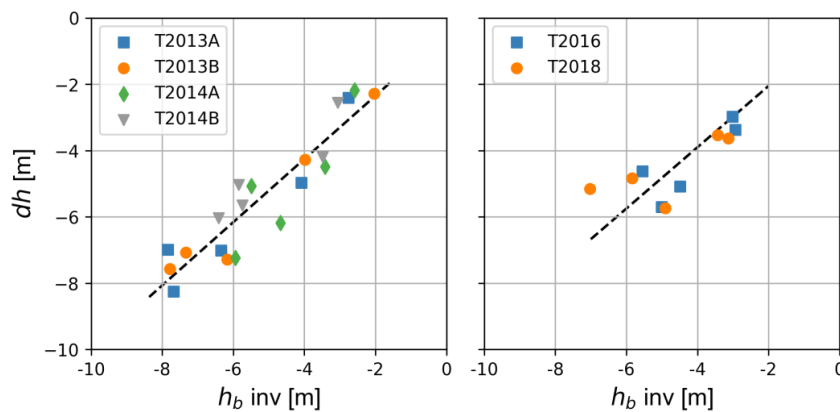


**Figure 8.** Elevation difference ( $dh$ ) TDM DEM - REMA versus the computed elevation bias, derived from the volumetric coherence for the snow pit sites P1 to P5. - - - linear regression line.

Maps of  $dh$  and the computed TDM elevation bias are shown in Fig. 9 for scene T2013B and in Fig. 10 for scene T2016. These two scenes have almost the same vertical wavenumber but different incidence angles. The differences between HH and VV polarized data of the T2016, respectively T2018, scene are insignificant. We use the mean value of the HH and VV based DEMs of the single dates for the comparison in order to reduce the impact of random phase noise. In Table 3 mean numbers over the LGA are specified for  $dh$ ,  $h_{bInv}$  and  $\gamma_{Vol}$ , the coefficient of determination ( $R^2$ ) for linear correlation between  $dh$  and  $h_{bInv}$  and the root-mean square difference (RMSD). The numbers for  $R^2$  and RMSD refer to the maps resampled to 8 m grid size, low-pass filtered over  $7 \times 7$  pixels windows using a Gauss function. The  $dh$  value of the TDMgl DEM ( $dh = 5.61 \text{ m}$ ) differs only by 0.06 m from the mean  $dh$  of the T2013/14 data. The TDMgl DEM is based on several TDM scenes acquired in 2013 and 2014. The  $dh$  map for TDMgl vs. REMA shows a similar spatial pattern as  $dh$  of the individual DEMs (Fig. S2).

As for the snow pit sites, the mean values over the LGA show distinct differences in  $dh$ ,  $h_{bInv}$  and  $\gamma_{Vol}$  between the data sets with different incidence angle. The magnitudes of the elevation bias of the T2013/14 data (mean  $dh = -5.55 \text{ m}$ ,  $h_{bInv} = -5.22 \text{ m}$ ) are larger than the corresponding values of the T2016/18 data set ( $dh = -4.59 \text{ m}$ ,  $h_{bInv} = -4.79 \text{ m}$ ). As for the snow pit sites, this is opposite to the expectation for a uniform isotropic scattering medium for which  $|h_b|$  should be larger in scenes with smaller off-nadir angles in case of the same value of  $H_a$ .

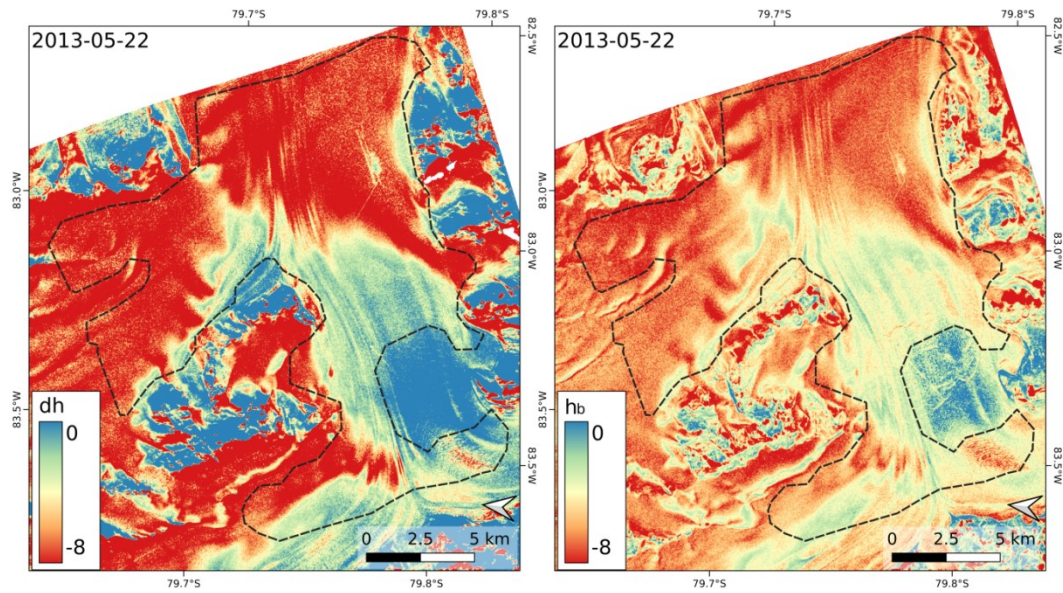
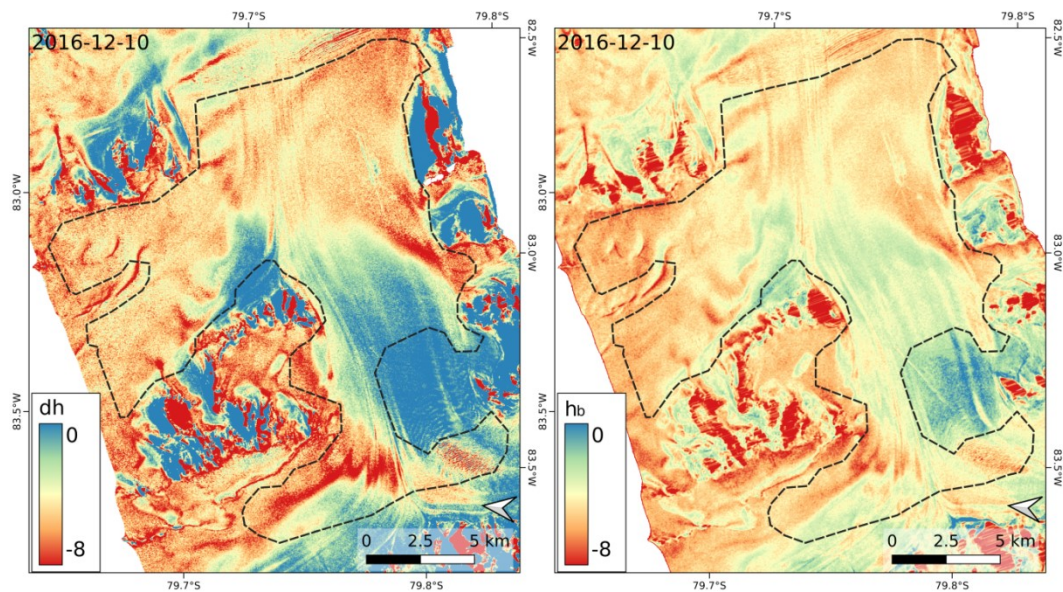


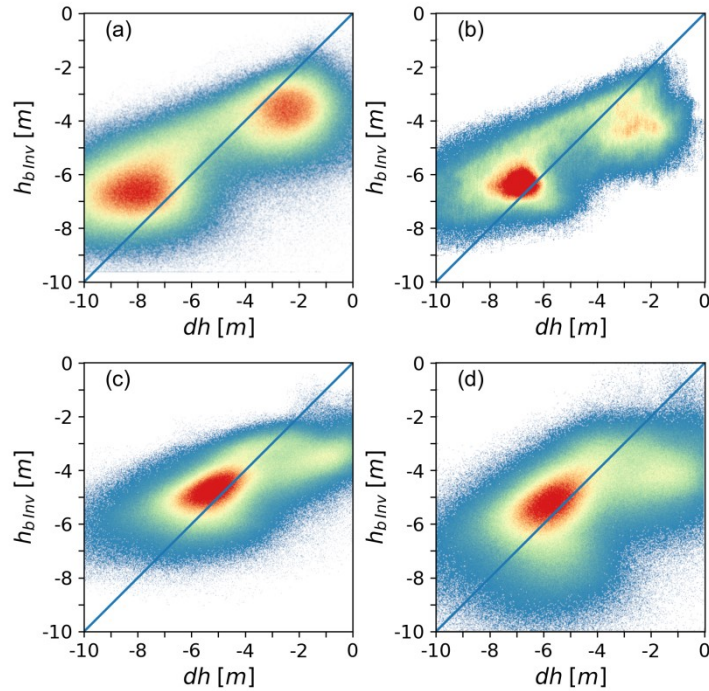
**Figure 9.** Elevation difference (dh) TDM DEM – REMA and elevation bias ( $h_{bInv}$ ) by inversion of  $\gamma_{Vol}$  for the TDM scene 22 May 2013 ( $\theta_i = 38.6^\circ$ ). The outline encloses the LGA.



530 **Figure 10.** Elevation difference (dh) TDM DEM – REMA and elevation bias ( $h_{bInv}$ ) by inversion of  $\gamma_{Vol}$  for the TDM scene 10 December 2016 ( $\theta_i = 21.6^\circ$ ), based on HH and VV polarized data.

The LGA mean values of dh and  $h_{bInv}$  show minor differences: -0.33 m for T2013/14 and 0.20 m for T2016/18. The spatial patterns of dh and  $h_{bInv}$  are similar, but the mean slope of the 2D distribution deviates from the 1:1 correspondence (Fig. 11). The magnitude of the computed elevation bias is overestimated over the areas with coarse grained firm and small penetration depth in the surroundings of the BIA and underestimated in areas of higher accumulation rate. These depth dependent deviations can, at least partly, be attributed to the simplified assumption of the uniform volume approach.

535



540 **Figure 11.** Scatterplot of the elevation difference TDM DEM minus REMA ( $dh$ ) vs. the computed elevation by inversion of  $\gamma_{vol}$  ( $h_{b,inv}$ ) on Union Glacier LGA. (a) TDM scene 22 May 2013; (b) mean of the T2013 and T2014 scenes; (c) 10 December 2016 and (d) 10 January 2018, mean values of VV and HH channels. The line shows the 1:1 correspondence. The colour code represents the 2D data density.

## 6. Discussion

545 A critical issue for inverting interferometric coherence in terms of the InSAR elevation bias is the description of the vertical backscattering profile in the snow volume. A simple model is required, in particular if only single channel backscatter data are available. We apply the model of Dall (2007) in which the vertical backscatter function is defined by the extinction coefficient of a uniform random volume accounting for the combined effect of absorption and scattering. In order to check the suitability of this model for describing the backscattering profile of layered polar firn, we performed backscatter simulations for the snow pit sites with a multilayer radiative transfer model (Appendix).  
550

The computed total  $\sigma^\circ$  values at  $\theta_i = 40^\circ$  are matching the observed total backscatter intensities of the T2013/14 scenes for snow pit sites 2 to 5. The simulated vertical backscatter profiles and the exponential profiles of the uniform volume approach show close agreement for sites 2 to 4. The variations between individual layers, tracing back to accumulation and wind erosion events as well as to seasonal effects, are suppressed in the vertical profile of the cumulative backscatter contributions. At sites 2 to 4 the uniform volume approach shows minor overestimation of the backscatter contributions from the top snow layers due to the assumption of a constant scattering coefficient whereas the actual grain size in the near-surface layers is below average. This effect is more pronounced at pit 5 where the layers with small grains reach down to 1.4 m depth.  
555

On the other hand, the radiative transfer simulations at  $\theta_i = 22^\circ$ , referring to the T2016/18 scenes, yield underestimation of  $\sigma^\circ$  by several dB. For pit 1 the simulated backscatter intensity is underestimated also at  $\theta_i = 40^\circ$ . The incidence angle differences (Fig. 5) are most pronounced in the glacier zones with comparatively high  
560

accumulation. The radiative transfer model used for the simulations computes volume scattering for bi-continuous, random structures applying the improved Born Approximation and assumes plane-parallel, homogenous layers (Picard et al., 2018). As a matter of fact, in addition to incoherent volume scatter the contributions of rough internal interfaces as well as interlayer interferences play a role (Tan et al., 2017; Fischer et al., 2019a).

The most likely explanation for the increased backscatter towards near-nadir incidence is the increased scattering at interfaces between layers of different density and wind-packed structures. In particular on the main section of Union Glacier the snow surfaces are wind roughened, showing elongated sastrugi at the metre scale with ripples of centimetres vertical extent. The surface roughness related to wind packing and erosion is also evident in snow pits at interfaces between snow layers and at wind crusts. Ashcraft and Long (2006) attribute the backscatter anisotropy, observed in scatterometer data of katabatic wind zones, to the anisotropy in the preferential roughness direction of the snow surface and of internal interfaces. Such behaviour was also observed for density stratified firn on the East Antarctic Plateau and reproduced by simulations with a layered-medium radiative transfer model (Rott et al., 1993; West et al., 1996).

Whereas differential propagation effects lead to distinct co-polarization differences in the phase and magnitude of the complex co-polarized (HH-VV) coherence, the differences in the interferometric coherence and derived penetration bias between the individual polarizations are insignificant (Table 3). This implies that the vertical backscatter distributions of the co-polarizations channels are similar. Consequently, the data from HH and VV polarization can be combined for estimating the elevation bias, reducing the impact of noise. The differences in  $\sigma^\circ$  between HH and VV polarization are also small, as to be expected for low incidence angle data (Fung, 1994). On the average over the LGA  $\sigma^\circ_{HH}$  is higher by 0.2 dB compared to  $\sigma^\circ_{VV}$  and there is no distinct spatial variability.

We checked also the information content of the phase,  $\phi_{HH-VV}$ , and magnitude,  $|\gamma_{HH-VV}|$ , of the complex HH-VV polarized correlation coefficient regarding potential contributions in support of elevation bias retrievals. Measurements with a ground-based (Jordan et al., 2019) and an airborne (Dall, 2009) polarimetric ice sounder in the dry snow zone of Greenland show major variations of  $\phi_{HH-VV}$  related to anisotropic scattering at internal interfaces and to the crystal orientation of ice fabrics. Leinss et al. (2016) derived  $\phi_{HH-VV}$  from TerraSAR-X and ground-based scatterometer data in order to determine the dielectric and structural anisotropy of seasonal snow, showing distinct differences in  $\phi_{HH-VV}$  related to the snow microstructure. We computed the complex co-polarized correlation coefficient from data of the T2016 scene, using estimation windows comprising about 125 independent samples (Fig. S3). The co-polarized coherence,  $|\gamma_{HH-VV}|$  reflects to some degree the spatial pattern of the elevation bias. On the BIA  $|\gamma_{HH-VV}|$  is 0.92, in the low accumulation areas near the BIA 0.6 to 0.7, and in the vicinity of the ALE camp 0.3 to 0.5. On the LGA the linear correlation coefficient,  $R^2$ , between  $|\gamma_{HH-VV}|$  and dh amounts to 0.29. Reduced coherence can be attributed to decorrelation by the non-coherent scattering components in the volume.

The mean co-polarized phase difference,  $\phi_{HH-VV}$ , of the BIA is close to zero (0.05 rad), as to be expected for backscatter from a comparatively smooth surface. On the LGA (snow and firn) the mean value of  $\phi_{HH-VV}$  amounts to 0.50 rad with a high standard deviation (0.39 rad) because the ensemble comprises positive as well as negative values. Positive phase differences, an indication for anisotropic scattering at horizontal structures such

as internal interfaces, are dominating on the main glacier. A substantial part of Driscoll Glacier shows negative  $\phi_{\text{HH-VV}}$  values, the reason for which is unclear. On LGA  $R^2$  between  $\phi_{\text{HH-VV}}$  (comprising positive and negative values) and  $dh$  is close to zero, whereas  $R^2$  for the magnitude of the phase difference,  $|\phi_{\text{HH-VV}}|$ , is 0.19. These observations are an indication for differential propagation effects between HH and VV polarized waves in the snow/ firn volume, but the sources of the anisotropy are not uniquely defined. In order to assess the value of the complex co-polarized correlation coefficient for supporting retrievals of the penetration-related elevation bias dedicated studies are needed, employing preferably multi-incidence angle observations.

According to theory the penetration bias and phase centre depth at a given frequency and polarization change with the baseline and the incidence angle (Dall, 2007). This was verified with airborne data by Fischer et al. (2020), showing that the changes are significant in particular at small volumetric wavenumbers (long baselines). This is evident comparing two scenes with almost the same incidence angle: T2016 ( $\theta_i = 21.6^\circ$ ,  $k_{z\text{Vol}} = 0.120$ ) and T2018 ( $\theta_i = 22.1^\circ$ ,  $k_{z\text{Vol}} = 0.072$ ). Both the  $dh$  and  $h_{\text{blnv}}$  values indicate deeper penetration for T2018 compared to T2016, amounting on the LGA to  $dh = -4.80$  m for T2018 versus  $-4.38$  m for T2016, respectively to  $h_{\text{blnv}} = -5.18$  m for T2018 versus  $-4.40$  m for T2016 (Table 3).

For a uniform scattering medium deeper penetration is expected for a steeper propagation path (lower incidence angle). This can be checked by comparing two scenes with almost the same vertical wavenumber and different incidence angles: T2013B ( $\theta_i = 38.6^\circ$ ,  $k_{z\text{Vol}} = 0.121$ ,  $dh(\text{LGA}) = -5.63$  m) and T2016 ( $\theta_i = 21.6^\circ$ ,  $k_{z\text{Vol}} = 0.120$ ,  $dh(\text{LGA}) = -4.38$  m). However, assuming for T2016 a volume with the same scattering and absorption coefficients as for T2013B, the expected elevation bias for T2016 is  $-6.04$  m. The same behaviour is evident for the mean  $dh$  values of the snow pit sites ( $\langle dh \rangle = -5.70$  m for T2013B,  $\langle dh \rangle = -4.35$  m for T2016). This mismatch points also to increased scattering at internal interfaces at low incidence angles, as concluded from backscatter modelling (see Appendix).

The impact of the incidence angle on the mean difference between the observed  $dh$  and the computed  $h_{\text{blnv}}$  is comparatively small. For T2103/14 the mean value for  $dh - h_{\text{blnv}}$  amounts to  $-0.33$  m, for T2016/18 to  $0.20$  m (Table 3). This shows that the uniform volume approach, based on the volumetric coherence, delivers reasonable mean penetration corrections. However, biases for deep, respectively shallow, penetration indicate systematic deviations from the uniform volume approach. In the first case the smaller grain size of the top snow layers causes a shift of the scattering phase centre to larger depth compared to exponential extinction. The second case, an overestimation of  $h_b$  in wind exposed low accumulation zones, can be attributed to the larger size of the scattering elements and a denser sequence of internal interfaces.

## 7. Conclusion

In this study we investigated the feasibility for estimating the penetration-related elevation bias of interferometric topographic products over snow and ice by inverting the volumetric coherence. Single-pass across-track SAR interferometry has been widely applied for comprehensive, spatially detailed measurements of glacier and ice sheet topography as the measurements are not impaired by temporal decorrelation of the interferometric signal, variations in atmospheric propagation conditions, cloudiness, and variable illumination. A main concern for the use of InSAR DEMs over glaciers and ice sheets is the correction of the elevation bias. A common approach is the use of laser altimetry data as reference for vertical co-registration (e.g. Abdullahi et al.,

2019, Rizzoli et al., 2017a; 2017b; Wessel et al., 2016). However, altimetry data often lack the required temporal  
640 coincidence and coverage for comprehensive corrections.

We applied and evaluated the method of Dall (2007) for deriving the elevation bias of dry polar snow and firn by  
inverting the volumetric coherence of X-band InSAR data of the TanDEM-X mission. This method is based on  
the assumption of a uniform volume with constant scattering and absorption properties whereas actual snow/firn  
volumes show depth-dependent changes of the density and the scattering elements, as well as variations at small  
645 vertical scale related to stratification. The use of a simple model is required because the inversion of a single  
parameter does not allow the representation of the complex layered structure. The study area, Union Glacier in  
Antarctica, comprises ice-free surfaces, bare ice and dry snow and firn with different structural properties  
depending on wind exposure and accumulation, a suitable environment for studying the performance of the  
inversion algorithm. For the statistical analysis we focussed at the level glacier area, including sites of field  
650 measurements, in order to minimize the impact of possible errors in SAR image co-registration with optical  
reference data.

The TanDEM-X data set comprises interferometric pairs with different interferometric baselines, as well as with  
two distinctly different incidence angle ranges. This enables to study the impact of these parameters on the  
computed elevation bias. In spite of the simplified representation of the vertical backscatter profile the inversion  
655 according to the model of Dall (2007) provides reasonable estimates. The mean values of the computed elevation  
bias over the level glacier area, derived from data of the different TDM scenes, range from -4.4 m to -5.8 m,  
varying with the baseline and incidence angle. The mean differences between the computed penetration bias and  
the estimates based on differencing of optical and TDM DEMs range from 0.40 m to -0.64 m for the different  
scenes. There is a trend for overestimation of the elevation bias in areas that are subject to high wind exposure  
660 and low accumulation rates and for underestimation in areas with higher accumulation. In both cases deviations  
from the uniform volume structure are the main reason. In the first case the dense sequence of horizontal  
structures related to internal wind crusts, ice layers and density stratification causes increased scattering in the  
near-surface layers. In the second case the smaller grain size of the top snow layers causes a downward shift of  
the scattering phase centre compared to the uniform volume approach.

665 Advancements for the estimation of the InSAR elevation bias can be expected from progress in the  
representation of snow/firn structural properties in models for radar signal propagation. After all, the derivation  
of the interferometric elevation bias from volumetric coherence is a promising option which should be carried  
forward as it delivers spatially detailed information coinciding both in space and time with the topographic  
products. Fischer et al. (2020) analysed deviations from the uniform volume approach for airborne multi-  
670 frequency polarimetric SAR data. They explored sources and interaction mechanisms responsible for these  
deviations and tested different models for vertical backscatter contributions, concluding that in case of single  
polarization data the inversion based on the uniform volume model is a preferred approach. Beyond that, Fischer  
et al. (2019b) demonstrated the added value of multi-baseline polarimetric InSAR data for deriving the depth of  
dominant scattering layers in polar firn, key information for locating the position of the scattering phase centre  
675 within the volume. Consequently, further progress on InSAR signal penetration in layered media can be expected  
from the use of polarimetric data as well as from multi-baseline and multi-angle observations.

## **Appendix: Representation of the vertical backscatter profile**

In order to assess the suitability of the vertical backscatter distribution of the uniform volume approach we performed backscatter simulations with a multilayer radiative transfer (RT) model. According to the RT theory the normalized radar cross section scattered back from depth  $z$  of a random scattering medium and received at the surface can be described by:

$$\sigma^0(z) = T^2(\theta_i) \sigma_v^0(z) \exp \left\{ 2 \int_z^0 \left[ \frac{k_e(z)}{\cos \theta_r} \right] dz \right\} \quad (\text{A1})$$

$T$  is the transmissivity at the air/snow interface,  $\sigma_v^0$  is the volume scattering coefficient,  $k_e$  is the volume extinction coefficient accounting for scattering and absorption losses.  $\theta_i$  is the incidence angle at the surface,  $\theta_r$  is the refracted incidence angle;  $z$  within the medium is negative. The factor 2 accounts for the two-way travel path in the volume. The uniform volume approach assumes constant scattering and extinction properties (Hoen and Zebker, 2000). The resulting vertical backscatter function, accounting for two-way losses, is given by

$$\sigma^0(z) = \langle \sigma_v^0 \rangle \exp \left( \frac{2z k_e}{\cos \theta_r} \right) = \langle \sigma_v^0 \rangle \exp \left( \frac{2z}{d_p} \right) \quad (\text{A2})$$

$\langle \sigma_v^0 \rangle$  is the average normalized volume scattering cross section,  $d_p$  is the one-way power penetration depth.

We performed backscatter simulations for the snow pit sites with the multilayer Snow Microwave Radiative Transfer (SMRT) thermal emission and backscatter model of Picard et al. (2018). The SMRT offers a choice of different electromagnetic and microstructure models for computing the scattering and absorption coefficients and the scattering phase function in a given layer. We used the sticky hard sphere (SHS) model for characterizing the microstructure and the improved Born approximation for computing volume scattering and absorption. Input parameters for describing the microstructure of each layer with the SHS model are the snow density, the temperature, the effective grain size and the stickiness. The effective grain size refers to the maximum axis length of the prevailing snow grains in each layer (Fierz et al., 2009). Down to the bottom of the snow pits the grain size and density data are based on the field measurements. The increase of snow density below is adopted from the density profile of the firn core GUPA-1 of Hoffmann et al. (2020). For estimating the increase of grain size with depth below snow pit depth we apply the grain growth model of Linow et al. (2012).

The stickiness parameter,  $\tau$ , is used in the SHS models to account for sintering and clustering of snow grains, forming aggregates that are larger than individual grains. The collective scattering and wave interaction effects of the aggregates result in increased scattering compared to individual grains and show a different phase function with more forward scattering. Löwe and Picard (2015) found stickiness to be an essential parameter when modelling snow as a sphere assembly. They show that the stickiness parameter can be objectively estimated from micro-tomography images. However, objective methods for deriving the stickiness parameter from field observations are pending. Typical stickiness values for X-band backscatter simulation of coarse-grained metamorphic snow are  $\tau = 0.1$ , whereas  $\tau = 1.0$  is similar to the non-sticky case (Chang et al., 2014). We use  $\tau$  as tuning parameter in order to match the average observed and the computed total backscatter intensity at the individual sites. The  $\tau$ -values range from  $\tau = 0.1$  for layers with large grains and clusters to  $\tau = 0.2$  for near surface layers. The computations were performed down to 20 m depth. Contributions to total backscatter from the layers below are negligible because of the dense medium effect and the attenuation in the layers above.

Whereas the stickiness parameter accounts for increased scattering due to bonding, the close packing of particles introduces near field interactions causing reduced scattering (Tsang et al., 2013). Compared to the assumption of



715 independent scattering elements the scattering in a dense medium decreases with increasing volume fraction of  
the scatterers larger than about 0.2. We performed test runs with the dense medium RT model with the Quasi-  
Crystalline Approximation of Mie Scattering (DMRT-QMS) of Tsang et al. (2007) and Chang et al. (2014) using  
the same stickiness and grain sizes parameters as for the computations with the Improved Born approximation  
approach of SMRT using the SHS microstructure parameterization. The results of both models are in close  
720 agreement and point out that the parameterization of snow microstructure is decisive for snow backscatter  
simulations.

Fig. A1 shows vertical profiles of the power scattered back from the volume below a specific depth as fraction of  
the total power observed at the surface, both for multilayer RT modelling results and the uniform volume (UV)  
approach. The RT computations refer to  $\theta_i = 40^\circ$ , the mean local incidence angle at the snow pit sites of the  
725 T2013/14 scenes. The extinction coefficient for the exponential UV function is based on the mean penetration  
depth which is deduced from the mean elevation difference (dh) between the T2013/14 scenes and the REMA  
assuming that the 2-way penetration depth is equal to the elevation bias.

Layers with coarse grains and grain clusters show higher backscatter coefficients but are thinner than compact  
layers of higher density such as wind slabs. The variations between individual layers with different scattering  
730 properties are smoothed out in the depth-dependent backscatter function. Consequently, the exponential  
function is able to reproduce the vertical backscatter profiles quite well. The reduced backscatter contributions  
from near surface layers shown by the RT model can be attributed to the smaller grain size whereas the UV  
model assumes constant scattering cross section. This effect yields for pits 2, 3 and 4 only minor differences  
between the two models. At pit 5 the differences are more pronounced due to the smaller grain size of the top  
735 layers related to the higher accumulation rate.

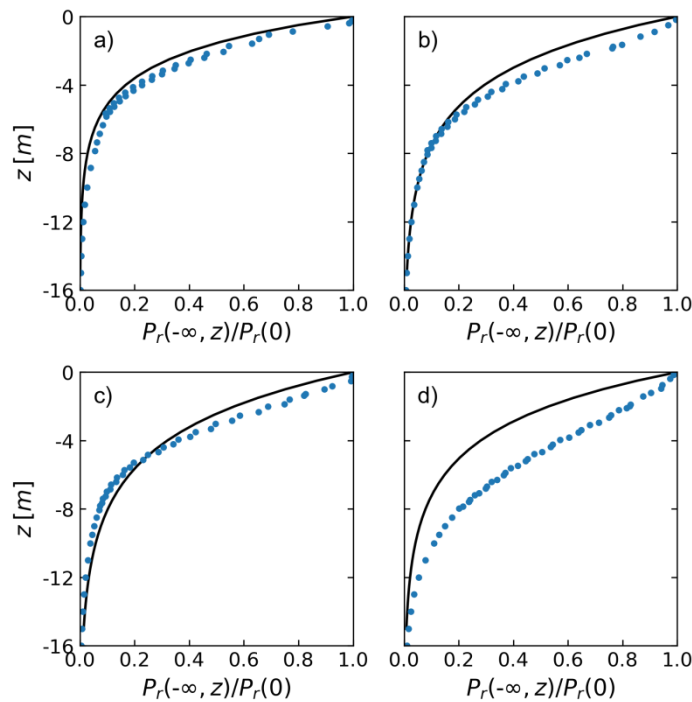


**Figure A1.** Fraction of X-band HH-polarized power scattered back from the snow/finn volume below the depth  $z$ . Points: RT model computations for individual layers. Curve: Model for exponential extinction. Input parameters refer to Union Glacier Pit 2 (a), Pit 3 (b), Pit 4 (c) and Pit 5 (d).

740 The RT simulations for  $\theta_i = 40^\circ$ , using  $\tau$  as tuning parameter, reproduce exactly the observed total mean backscatter intensity of the corresponding T2013/14 data at snow pit sites 2 to 5. For pit 1 the simulations for  $\theta_i = 40^\circ$  yield an underestimation of 3 dB, even when assuming consistently maximum stickiness ( $\tau = 0.1$ ), very likely due to neglect of the enhanced scattering contributions of ice layers and wind crusts. The RT simulations for  $\theta_i = 22^\circ$ , corresponding to the T2016/18 incidence angle, show underestimation throughout. The simulations  
745 for pit 2 to pit 5 show from  $40^\circ$  to  $22^\circ$  incidence angle an average  $\sigma^\circ$  increase of 1.3 dB, whereas the observed increase is 5.9 dB. Large incidence angle dependence of backscatter is typical for density-layered firn. Ground-based X-band scatterometer measurements at several sites in the dry snow zone of Dronning Maud Land with accumulation rates between  $130$  and  $260 \text{ kg m}^{-2} \text{ a}^{-1}$ , comparable to those on Union Glacier, show from  $40^\circ$  to  $20^\circ$  incidence angle a mean  $\sigma^\circ$  increase of 6.5 dB (Rott et al., 1993). The strong increase towards low off-nadir  
750 angles is an indication for increased scattering at horizontal structures such as rough interfaces between snow layers of different density and wind crusts whereas the RT model assumes plane-parallel layered structures.

*Data availability.* Interferometric satellite products processed for this study will be made available upon publication of the final version of the manuscript at <http://cryoportale.nveo.at/>.

755 *Supplement.* The supplement related to this article is available on-line.

*Author contributions.* HR conceived the study, performed the field work, was in charge of the data analysis and scientific interpretation and drafted the manuscript. SS, JW and LL contributed to backscatter analysis and numerical simulations, and to the analysis of topographic data. LK processed and calibrated the interferometric satellite data. All authors contributed to the data interpretation, discussion of the results and revision of the  
760 manuscript.

*Competing interests.* The authors declare that they have no conflict of interest.

*Acknowledgements.* The TanDEM-X data were made available by DLR through the projects XTI\_GLAC6809 and DEM\_GLA1059. The ICESat and ICESat-2 laser altimeter data were obtained from the NASA Distributed Active Archive Center, US National Snow and Ice Data Center (NSIDC), Boulder, Colorado. REMA data were  
765 downloaded from the U.S. Polar Geospatial Center. Landsat 8 images were downloaded from the United States Geological Survey (USGS) Landsat Archive. HR would like to thank Antarctic Logistics & Expeditions LLC (ALE) for perfect logistic support and for the provision of meteorological data and in particular Nate Opp for his active and knowledgeable support in the field work. The authors are very grateful to the editor Etienne Berthier and the two anonymous reviewers for constructive comments and suggestions, helping to improve the structure  
770 and clarity of the paper.

## References

- 775 Abdullahi, S., Wessel, B., Huber, M., Wendleder, A., Roth, A., and Kuenzer, C.: Estimating penetration-related X-Band InSAR elevation bias: A study over the Greenland Ice Sheet, *Remote Sens.*, 11, 2903, doi:10.3390/rs11242903, 2019.
- Alley, R. B.: Concerning the deposition and diagenesis of strata in polar firn, *J. Glaciol.*, 34 (118), 283 – 290, 1988.
- 780 Ashcraft, I. S., and Long, D. G.: Relating microwave backscatter azimuth modulation to surface properties of the Greenland Ice Sheet, *J. Glaciol.*, 52 (177), 257–266, 2006.
- Bamler, R. and Hartl, P.: Synthetic aperture radar interferometry, *Inverse Problems*, 14, R1 - R54, 1988.
- Breit, H., Fritz, T., Balss, U., Lachaise, M., Niedermeier, A., and Vonavka, M.: TerraSAR-X processing and products, *IEEE Trans. Geosci. Rem. Sens.*, 48 (2), 727–740, 2010.
- Brenner, A. C., DiMarzio, J. P., and Zwally, H. J.: Precision and accuracy of satellite radar and laser altimeter 785 data over the continental ice sheets, *IEEE Trans. Geosc. Rem. Sens.*, 45 (2), 321-331, 2007.
- Chang W., Tan, S., Lemmetyinen, J., Tsang, L., Xu, X., Li, X., and Yueh, S.: Dense media radiative transfer applied to SnowScat and SnowSAR, *IEEE J. Sel. Topics Applied Earth Obs. Rem. Sens.*, 7, (9), 3811-3825, 2014.
- Colbeck, S. C.: Theory of metamorphism of dry snow, *J. Geophys. Res.*, 88 (C9), 5475–5482, 1983.
- 790 Colbeck, S. C.: Snow-crystal growth with varying surface temperatures and radiation penetration, *J. Glaciol.*, 35 (119), 23-29, 1989.
- Courville, Z. R., Albert, M. R., Fahnestock, M. A., Cathles, L. M., and Shuman, C. A.: Impacts of an accumulation hiatus on the physical properties of firn at a low-accumulation polar site, *J. Geophys. Res.*, 112(F2), F02030 (doi: 10.1029/2005JF000429), 2007.
- 795 Dall, J.: Elevation bias caused by penetration into uniform volumes, *IEEE Trans. Geosc. Rem. Sens.*, 45 (7), 2319–2324, 2007.
- Dall, J.: Polarimetric ice sounding at P-band: First results, in *Proc. IEEE Int. Geosci. Remote Sens. Symp. (IGARSS)*, Cape Town, South Africa, Jul. 2009, pp. 1024–1027, 2009.
- Dall, J., Madsen, S. N., Keller, K., and Forsberg, R.: Topography and penetration of the Greenland Ice Sheet 800 measured with airborne SAR interferometry, *Geophys. Res. Letters*, 28 (9), 1703-1706, 2001.
- Fierz, C., Armstrong, R.L., Durand, Y., Etchevers, P., Greene, E., McClung, D. M., Nishimura, K., Satyawali, P. K., and Sokratov, S. A.: The International Classification for Seasonal Snow on the Ground, IHP-VII Technical Documents in Hydrology No. 83, IACS Contribution No. 1, UNESCO-IHP, Paris, 2009.
- Fischer, G., Papathanassiou, K. P., and Hajnsek, I.: Modeling multifrequency Pol-InSAR data from the 805 percolation zone of the Greenland Ice Sheet, *IEEE Trans. Geosc. Rem. Sens.*, 57 (4), 1963–1976, 2019a.
- Fischer, G., Jäger, M., Papathanassiou, K. P., and Hajnsek, I.: Modeling the vertical backscattering distribution in the percolation zone of the Greenland Ice Sheet with SAR tomography, *IEEE J. Sel. Topics Applied Earth Obs. Rem. Sens.*, 12 (11), 4839 – 4405, 2019b.
- Fischer, G., Papathanassiou, K. P., and Hajnsek, I.: Modeling and compensation of the penetration bias in InSAR 810 DEMs of ice sheets at different frequencies, *IEEE J. Sel. Topics Applied Earth Obs. Rem. Sens.*, 13 (5), 2698-2707, 2020.
- Forsberg, R., Keller, K., Nielsen, C. S., Gundestrup, N., Tscherning, C. C., Madsen, N. S., and Dall, J.: Elevation change measurements of the Greenland Ice Sheet, *Earth Planet. Space*, 52, 1049-1053, 2000.

- 815 Fung, A. K.: Microwave Scattering and Emission Models and Their Applications, Artech House, Boston,  
London, 1994.
- Hoen, E. W., and Zebker, H. A.: Penetration depths inferred from interferometric volume decorrelation observed  
over the Greenland Ice Sheet, *IEEE Trans. Geosc. Rem. Sens.*, 38(6), 2571-2583, 2000.
- Hoen, E. W., and Zebker, H. A.: Correction to: Penetration depths inferred from interferometric volume  
decorrelation observed over the Greenland Ice Sheet, *IEEE Trans. Geosc. Rem. Sens.*, 39 (1), p. 215, 2001.
- 820 Hoffmann, K., Fernandoy, F., Meyer, H., Thomas, E. R., Aliaga, A., Tetzner, D., Freitag, J., Opel, T., Arigony-  
Neto, J., Göbel, C. F., Jaña, R., Rodríguez Oroz, D., Tuckwell, R., Ludlow, E., McConnell, J. R., and  
Schneider, C.: Stable water isotopes and accumulation rates in the Union Glacier region, West Antarctica  
over the last 35 years, *The Cryosphere*, 14, 881–904, 2020.
- Howat, I. M., Porter, C., Smith, B. E., Noh, M.-J., and Morin, P.: The Reference Elevation Model of Antarctica,  
825 *The Cryosphere*, 13, 665-674, 2019.
- Jordan, T. M., Schroeder, D. M., Castelletti, D., Li, J., and Dall, J.: A polarimetric coherence method to  
determine ice crystal orientation fabric from radar sounding: Application to the NEEM ice core region, *IEEE  
Trans. Geosc. Rem. Sens.*, 57 (11), 8641 – 8657.
- Krieger, G., Moreira, A., Fiedler, H., Hajnsek, I., Werner, M., Younis, M., and Zink, M.: TanDEM-X: A satellite  
830 formation for high resolution SAR interferometry, *IEEE Trans. Geosc. Rem. Sens.*, 45 (11), 3317–3341,  
2007.
- Krieger, G., Zink, M., Bachmann, M., Bräutigam, B., Schulze, D., Martone, M., Rizzoli, P., Steinbrecher, U.,  
Anthony, J. W., De Zan, F., Hajnsek, I., Papathanassiou, K., Kugler, F., Rodriguez Cassola, M., Younis, M.,  
Baumgartner, S., Lopez Dekker, P., Prats, P., and Moreira, A.: TanDEM-X: a radar interferometer with two  
835 formation flying satellites, *Acta Astronaut.*, 89, 83–98, doi:10.1016/j.actaastro.2013.03.008, 2013.
- Lei, Y., Siqueira, P., and Treuhart, R.: A dense medium electromagnetic scattering model for the InSAR  
correlation of snow, *Radio Sci.*, 51, 461–480, doi:10.1002/2015RS005926, 2016.
- Linow, S., Hörhold, M. W., and Freitag, J.: Grain-size evolution of polar firn: a new empirical grain growth  
parameterization based on X-ray microcomputer tomography measurements, *J. Glaciol.*, 58 (212), 1245 –  
840 1252, 2012.
- Leinss, S., Löwe, H., Proksch, M., Lemmetyinen, J., Wiesmann, A., and Hajnsek, I.: Anisotropy of seasonal  
snow measured by polarimetric phase differences in radar time series, *The Cryosphere*, 10, 1771–1797,  
<https://doi.org/10.5194/tc-10-1771-2016>, 2016.
- Löwe, H., and Picard, G.: Microwave scattering coefficient of snow in MEMLS and DMRT-ML revisited: the  
845 relevance of sticky hard spheres and tomography-based estimates of stickiness, *The Cryosphere*, 9, 2101–  
2117, 2015.
- Mätzler, C.: Microwave permittivity of dry snow, *IEEE Trans. Geosc. Rem. Sens.*, 34 (2), 573 – 581, 1996.
- Nuth, C., and Kääb, A.: Co-registration and bias corrections of satellite elevation data sets for quantifying glacier  
thickness change, *The Cryosphere*, 5, 271–290, <https://doi.org/10.5194/tc-5-271-2011>, 2011.
- 850 Picard, G., Sandells, M., and Löwe, H.: SMRT: an active–passive microwave radiative transfer model for snow  
with multiple microstructure and scattering formulations (v1.0), *Geosci. Model Dev.*, 11, 2763–2788, 2018.
- Rivera, A., Zamora, R., Rada, C., Walton, J., and Proctor, S.: Glaciological investigations on Union Glacier,  
Ellsworth Mountains, West Antarctica, *Ann. Glaciol.*, 51, 91–96, 2010.

- Rivera, A., Zamora, R., Jaña, R., and Oberreuter, R.: Recent ice dynamic and surface mass balance of Union  
855 Glacier in the West Antarctic Ice Sheet, *The Cryosphere*, 8, 1445–1456, 2014.
- Rizzoli, P., Martone, M., Rott, H., and Moreira, A.: Characterization of snow facies on the Greenland Ice Sheet  
observed by TanDEM-X interferometric SAR data, *Remote Sens.*, 9 (4), 315; doi:10.3390/rs9040315, 2017a.
- Rizzoli, P., Martone, M., Gonzalez, C., Wecklich, C., Tridon, D. B., Bräutigam, B., Bachmann, M., Schulze, D.,  
Fritz, T., Huber, M., Wessel, B., Krieger, G., Zink, M., and Moreira, A.: Generation and performance  
860 assessment of the global TanDEM-X digital elevation model, *ISPRS J. Photogramm. Remote Sens.*, 132,  
119–139, 2017b.
- Rossi, C., Rodriguez Gonzalez, F., Fritz, T., Yague-Martinez, N., and Eineder, M.: TanDEM-X calibrated Raw  
DEM generation, *ISPRS J. Photogrammet. Remote Sens.*, 73, 12 - 20, doi: 10.1016/j.isprsjprs.2012.05.014,  
2012.
- 865 Rott, H., Sturm, K., and Miller, H.: Active and passive microwave signatures of Antarctic firn by means of field  
measurements and satellite data, *Ann. Glaciol.*, 17, 337-343, 1993.
- Smith, B., Fricker, H. A., Gardner, A., Siegfried, M. R., Adusumilli, S., Csathó, B. M., Holschuh, N., Nilsson, J.,  
Paolo F. S., and the ICESat-2 Science Team: *ATLAS/ICESat-2 L3A Land Ice Height, Version 2*, subset:  
ATL06\_ATLAS/ICESat-2 L3A Glacier Elevation/Ice Sheet Elevation (HDF5). Boulder, Colorado, USA.
- 870 NSIDC: National Snow and Ice Data Center, <https://doi.org/10.5067/ATLAS/ATL06.002> (date accessed: 25  
June 2019), 2019a.
- Smith, B., Fricker, H. A., Holschuh, N., Gardner, A. S., Adusumilli, S., Brunt, K. M., Csatho, B., Harbeck, K.,  
Huth, A., Neumann, T., Nilsson, J., and Siegfried, M. R.: Land ice height-retrieval algorithms for NASA's  
ICESat-2 photon-counting laser altimeter, *Remote Sens. Environ.*, 190, 260-273, 2019b.
- 875 Tan, S., Zhu, J., Tsang, L., and Nghiem, S. V.: Microwave signatures of snow cover using numerical Maxwell  
equations based on discrete dipole approximation in bicontinuous media and half-space Dyadic Green's  
function, *IEEE J. Sel. Topics Applied Earth Obs. Rem. Sens.*, 10 (11), 4686-4702, 2017.
- Tsang, L., Pan, J., Liand, D., Li, Z., Cline, D. W., and Tan, Y.: Modeling active microwave remote sensing of  
snow using dense medium radiative transfer (DMRT) theory with multiple-scattering effects, *IEEE Trans.*  
880 *Geosci. Rem. Sens.*, 45 (4), 990-1004, 2007.
- Tsang, L., Ding, K. H., Huang, S., and Xu, X: Electromagnetic computation in scattering of electromagnetic  
waves by random rough surface and dense media in microwave remote sensing of land surfaces, *Proc. IEEE*,  
101 (2), 255–279, 2013.
- Uribe, J., Zamora, R., Gacitúa, G., Rivera, A., and Ulloa, D.: A low power consumption radar system for  
885 measuring ice thickness and snow/firn accumulation in Antarctica, *Ann. Glaciol.*, 55, 39–48, 2014.
- Wessel, B., Bertram, A., Gruber, A., Bemm, S., and Dech, S.: A new high-resolution elevation model of  
Greenland derived from TanDEM-X, in: *Proc. of the ISPRS Annals of the Photogrammetry, Remote Sensing  
and Spatial Information Sciences of the XXIII ISPRS Congress, Prague, Czech Republic, 12–19 July 2016*,  
9–16, 2016.
- 890 West, R. D., Winebrenner, D. P., Tsang, L., and Rott, H.: Microwave emission from density-stratified Antarctic  
firn at 6 cm wavelength, *J. Glaciol.*, 42 (140), 63-76, 1996.
- Zwally, H. J., Li, J., Brenner, A. C., Beckley, M., Cornejo, H. G., DiMarzio, J., Giovinetto, M. B., Neumann, T.  
A., Robbins, J., Saba, J. L., Yi, D., and Wang, W.: Greenland ice sheet mass balance: distribution of  
increased mass loss with climate warming, *J. Glaciol.*, 57 (201), 88–102, 2011.

895 Zwally, H. J., Schutz, R., Bentley, C., Bufton, J., Herring, T., Minster, J., Spinhirne, J., and Thomas, R.:  
*GLAS/ICESat L2 Global Land Surface Altimetry Data, Version 34*, subset: 0GLAH12 GLAS/ICESat L2  
Global Antarctic and Greenland Ice Sheet Altimetry Data (HDF5). Boulder, Colorado USA, NASA National  
Snow and Ice Data Center, Distributed Archive Center.  
<https://dx.doi.org/10.5067/ICESAT/GLAS/DATA125> (date accessed: 28 April 2017), 2014.

900